

Giant Dynamical Paramagnetism in the driven pseudogap phase of $\text{YBa}_2\text{Cu}_3\text{O}_{6+\chi}$

Marios H. Michael,^{1,*} Duilio De Santis,² Eugene A. Demler,³ and Patrick A. Lee⁴

¹*Max Planck Institute for the Structure and Dynamics of Matter, Luruper Chausse 149, 22761 Hamburg, Germany*
²*Physics and Chemistry Dept., Interdisciplinary Theoretical Physics Group, Palermo University, 90128 Palermo, Italy*

³*Institute for Theoretical Physics, ETH Zurich, 8093 Zurich, Switzerland*

⁴*Department of Physics, MIT, 77 Massachusetts Avenue, 02139 Cambridge, MA, USA*

(Dated: March 17, 2025)

In the past decade, photo-induced superconducting-like behaviors have been reported in a number of materials driven by intense pump fields. Of particular interest is the high- T_c cuprate $\text{YBa}_2\text{Cu}_3\text{O}_{6+\chi}$ (YBCO), where such effect has been reported up to the so-called pseudogap temperature $T^* \sim 300 - 400$ K. In a recent tour-de-force experiment, a transient magnetic field which is proportional to and in the same direction of an applied field has been observed outside the sample, suggestive of flux exclusion due to the Meissner effect. In this paper, we point out that the transient magnetic field could be explained by a model of bilayers of copper-oxygen planes with a *local* superconducting phase variable persisting up to the pseudo-gap temperature at equilibrium. Under pumping, the time evolution is described by a driven sine-Gordon equation. In the presence of an external magnetic field, this model exhibits a novel instability which amplifies the current at the edges of the bilayer formed by defects or grain boundaries, producing a giant paramagnetic magnetization in the same direction as the applied field. We show how this scenario can fit most of the available data. To the extent that this model can account for the data, we conclude that the experiments have the important consequence of revealing the presence of local pairing in the pseudogap phase. While the bulk of this paper addresses the experiment on YBCO, this work reveals a new instability in the sine-Gordon equation that is of fundamental interest, with potential applications such as providing a mechanism for amplifying external magnetic fields at ultra-fast time scales in Josephson devices.

1. INTRODUCTION

Developments in pump and probe experiments have ushered in a new era of ultra-fast control in condensed matter systems^{1–3}. Experimental evidence indicates that pumping materials with an intense laser pulse in the THz frequency region can unlock collective behaviour on ultra-fast time-scales, such as ferro-electricity⁴, magnetism^{5–8}, band structure topology⁹, charge ordering^{10,11} and superconductivity (SC)^{12–16}. A prominent example in this field is the case of driven high- T_c cuprate $\text{YBa}_2\text{Cu}_3\text{O}_{6+\chi}$ (YBCO)^{17–21}. Under a 20 THz (mid-IR) pulse, at $T > T_c$, in the so-called pseudogap phase, time-resolved linear reflectivity measurements have shown signatures similar to that of the low temperature superconducting state for the duration of a few picoseconds after pumping²². The effect is observed beyond room temperature, up to the so-called pseudogap temperature $T^* \sim 300 - 400$ K, and has rightfully attracted a great deal of attention^{23–31}.

The defining property of a superconductor is the Meissner effect, i.e., perfect diamagnetic screening of the external magnetic field. A key question is whether the reported transient superconductor-like state also exhibits Meissner-like behavior. A breakthrough experimental study along this direction was published recently³², examining the response of driven YBCO above T_c in the presence of an external magnetic field. Ref. 32 indeed reports the detection of a transient magnetic field outside the sample which scales roughly linearly with the applied field and is in the same direction. The transient field's magnitude is of order $10 \mu\text{T}$ for an applied field of 10

mT at 100 K. By analogy with the equilibrium Meissner effect, Fava et al. have interpreted this phenomenon as originating from flux being expelled from the bulk of the sample.

In this paper, we provide an alternative explanation which does not involve the Meissner effect. To motivate our perspective, we first note that no evidence of photo-induced SC-like behavior in YBCO has been reported for the in-plane conductivity, as opposed to other reported photo-induced superconductors such as the organic compound¹³ and $\text{La}_{2-x}\text{Ba}_x\text{CuO}_4$ ³³. The key experimental signatures are instead the out-of plane optical response and second harmonic generation due to Josephson plasmons^{18,19}, which involve current flow perpendicular to the planes. Since the Meissner effect would require a screening supercurrent to flow both in-plane and out-of-plane, we are motivated to seek an explanation of the recent magnetization data through a model which does not invoke a net in-plane supercurrent flow, but which accounts for the dynamical interlayer responses.

These considerations—elaborated further in Sec. 2—lead us to study the behavior of the relative phase θ that describes the Josephson current between two SC-like layers when driven by an intense AC electric field, as described by a driven sine-Gordon (SG) equation^{34–36}. We are quickly led to consider the highly nonlinear regime of the SG equation by the following estimate. Using the Josephson relation $\partial_t \theta = 2eV/\hbar$ and $V = Ed_1$, where d_1 is the separation between the layers, we find that θ rapidly increases during the drive and reaches the value $\gtrsim \pi$, for the pump field amplitude $E_0 = 2.5 \text{ MV/cm}$ and

frequency $\omega_p = 2\pi \times 20$ THz employed experimentally³². In other words, the pendulum *effectively* representing the system's dynamics goes over the top and becomes inverted due to the drive. Therefore, under the pumping parameters of the experiment, the SG equation is deep in the nonlinear regime and we expect instabilities to develop.

Our analysis reveals that, in the presence of an external magnetic field, the existence of short-range SC correlations in equilibrium far above T_c would give rise to strong amplification of the equilibrium diamagnetic current, but in the *opposite* direction, under strong laser driving. The impact of our work is twofold. We provide a microscopic theory that fits the experimental data in Ref. 32, with strong implications for the nature of the pseudogap phase in high- T_c cuprate superconductors. At the same time, we uncover a new instability of the SG model in the presence of a small static magnetic field and strong uniform AC drive. This phenomenon has not been noted before, and could be realized in a broad range of systems such as 2D hetero-structures, long Josephson junctions, as well as cold atoms experiments employing artificial gauge fields^{34–42}. The instability of the SG model is discussed in Sec. 3 and can be read independently of the rest of the paper, which focuses on the nonlinear dynamics of driven pseudogap YBCO.

Below we consider the pumping geometry implemented in the experiments of driven YBCO, illustrated in Fig. 1(a). The YBCO structure consists of strongly coupled Cu-O layers, separated by distance $d_1 = 4$ Å, which we refer to as bilayers. These bilayers are separated from each other by a larger distance $d_2 = 8$ Å. In Sec. 2, starting with a minimal set of assumptions concerning the existence of SC phase coherence at equilibrium above T_c , we map the electrodynamics of the pseudogap phase of YBCO to the SG model. In Sec. 3, we demonstrate that short-range superconducting coherence within a single bilayer of YBCO leads to a small diamagnetic susceptibility $|\chi_d| \sim 10^{-5}$, depicted in Fig. 1(b). The giant dynamical paramagnetic effect can be summarized as an instability of the SG model triggered locally in each bilayer by a strong laser drive, sketched in Fig. 1(c). Section 4 illustrates that the different bilayers are capacitively coupled to each other, resulting in dynamically amplified edge currents (and displacement currents), outlined in Fig. 1(d). The magnetic field generated by these currents is paramagnetic and it penetrates the entire sample at the speed of light. The photo-generated paramagnetic response is proportional to the equilibrium diamagnetic response but can be orders of magnitude larger in amplitude. In Sec. 5, we discuss in detail how our theory compares with the experimental data. Finally, we conclude the paper with a discussion on other applications of our theory and its implications on the study of high T_c superconductors. An overview of our theoretical framework is given in the Methods section.

2. MODEL FOR DRIVEN PSEUDOGAP YBCO

Our starting assumption is that the phase of a SC order parameter can be defined locally in space and time up to the pseudogap temperature T^* , which we identify with a mean-field temperature T_{MF} . There is general agreement that phase fluctuations are responsible for the destruction of SC in cuprates above T_c ^{44,45}, driven by the BKT transition through the proliferation of vortices in each layer, even though the extent of the fluctuation regime is under debate. While the phase of each individual layer fluctuates wildly, the vortices between members of each bilayer are locked if the Josephson energy of a single bilayer is large enough^{46,47}. As a result, the *relative* phase θ between the layers does not see the vortices and can retain coherence, resulting in equal and opposite (counter-flow) supercurrents in the two members of the bilayer above T_c . This was demonstrated explicitly in a recent numerical study⁴⁸, which found coherence in the relative phase of bilayers and counter-flow supercurrent up to about twice T_c . We begin by studying in detail a model where θ is relatively small at equilibrium and its fluctuations are ignored. We uncover novel phenomena under strong driving, which we demonstrate to occur on a relatively short length-scale near the sample edge, so it is likely that local patches with small $\theta \bmod 2\pi$ are sufficient to see the effect. In 1D, we provide supporting evidence for this intuition in the Methods section by repeating our calculations in the presence of a soliton or an anti-soliton in the initial conditions. We will also offer an argument for the robustness of our mechanism against thermal fluctuations in 2D.

In YBCO, the Josephson tunnel coupling between members of the bilayers is much stronger than that between bilayers. We therefore introduce an intra-bilayer Josephson energy J_c , while the tunneling between bilayers is set to zero.

3. DYNAMICAL PHASE DIAGRAM OF THE DRIVEN SG MODEL

In a single bilayer, the relative phase between the two layers, $\theta(x, y, t)$, obeys the equation^{34–36} (see the derivation in the Appendix 1):

$$\partial_t^2 \theta + \frac{\sigma_n}{\epsilon_0} \partial_t \theta - \frac{c^2 \beta}{1 + \beta} \nabla^2 \theta + \omega_J^2 \sin \theta = \frac{e^* d_1}{\hbar} \partial_t E_p(t). \quad (1)$$

In Eq. (1) we include the electric field due to the pump pulse, which we parametrize as $E_p(t) = E_0 e^{-\frac{(t-t_p)^2}{2\sigma^2}} \sin[\omega_p(t-t_0)]$, where E_0 (ω_p) is the pump amplitude (frequency) and t_p , σ , and t_0 define, respectively, the center time, width, and starting time of the Gaussian envelope. We also introduce a damping term proportional to the DC normal state conductivity σ_n .

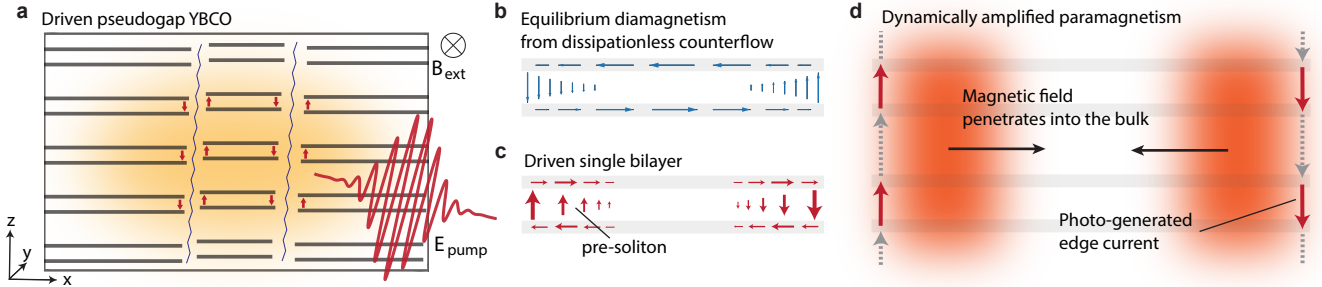


FIG. 1. **Schematic of Giant Dynamical Paramagnetism.** **a** Experimental set-up: the bilayer high- T_c cuprate YBCO is pumped with a pulse propagating along the y -axis, with the electric field polarised along the z -axis, over a spot size of about $100\ \mu\text{m}$ in diameter, in the presence of an external static magnetic field oriented along the y -axis. The sample consists of bilayers lying in the xy plane. It is broken up into finite segments by crystal defects, forming edges. Transient paramagnetic edge currents are generated at the boundaries due to the interplay between diamagnetic screening currents at the edges and Josephson nonlinear dynamics originating from short-range SC coherence in the pseudogap phase. **b, c** A single bilayer at equilibrium (b) and under a strong drive (c). (b) indicates that above T_c , even though long-range coherence and Meissner effect are absent, short-range fluctuating SC coherence within a single bilayer generates a Josephson current (colored in blue) between the two layers, leading to a small static diamagnetism, which we estimate from experiments⁴³ to be $\chi_d \sim -10^{-5}$. (c) illustrates that pumping a single bilayer gives rise to soliton-like excitations (dubbed ‘pre-solitons’ here) at the boundaries, characterized by large edge Josephson currents and localized in-plane counterflow currents. The (b)-(c) schematics show the difference between the current distribution in the pumped and equilibrium bilayer. **d** Upon pumping a YBCO multi-bilayer segment, in the presence of a magnetic field, the large paramagnetic edge Josephson currents in each bilayer (colored red) lead to displacement currents between bilayers (dotted grey). The overall edge current in the multi-bilayer segment generates a magnetic field that penetrates the entire segment at the speed of light, leading to a large magnetic flux inside the segment. The photo-generated edge currents lead to a large paramagnetic susceptibility that can be orders of magnitude larger than the equilibrium diamagnetic response.

The intra-bilayer Josephson plasma resonance frequency, ω_J , is given by the Josephson coupling, J_c , through the equation $\omega_J^2 = e^* d_1 J_c \epsilon_0 / \hbar$, and is set by the upper plasmon frequency in YBCO: $\omega_J = 2\pi \times 14\ \text{THz}$. The Josephson coupling determines the current along the z -direction, $j_z = J_c \sin \theta$. We introduce a dimensionless parameter

$$\beta = \frac{(e^*)^2 n_s d_1}{2\epsilon_0 m c^2} \quad (2)$$

which characterizes the counter-flow supercurrent. It is proportional to the 2D superfluid density of Cooper pairs in each layer, n_s ; ϵ_0 is the free space permittivity, m is the mass of a Cooper pair, c the speed of light in the material, and $e^* = 2e$ is the charge of a Cooper pair. We will soon see that its physical manifestation lie in the relation $\beta = -3\chi_d$, where χ_d is the diamagnetic susceptibility due to the SC fluctuations.

We consider the effect of an applied static field B_{ext} in the plane along the y direction, see Fig. 1(a). It is described by the boundary conditions (BC):

$$\partial_x \theta|_{x=0,L} = \frac{e^* d_1}{\hbar} B_{\text{ext}}, \quad (3)$$

where $x = 0$ ($x = L$) is intended as the left (right) edge of the bilayer segment. Since Eq. (3) depends only on x and the drive is uniform in space, we can consider solutions where θ is independent of y . In Eq. (1), the ∇ can be replaced by ∂_x and Eq. (1) simplifies to a one-dimensional

equation: the perturbed SG equation. The SG equation, as well as its perturbed counterparts, have been under intense investigation, and a great deal is known in the literature^{36,37}. What is less studied is the magnetic response under strong AC pulses, in the presence of an external magnetic field. We shall examine the interplay between strong pumping and the BC imposed by the external field given by Eq. (3) .

Equilibrium pseudogap diamagnetism. In equilibrium, Eqs. (1) and (3) lead to a diamagnetic response due to the presence of counter-flow supercurrents partially screening out the B_{ext} field within bilayers, see Fig. 1(b). The in-plane counter-flow supercurrent is given by the expression: $j_x = \frac{c^2 \epsilon_0 \hbar \beta}{e^* d_1 (1+\beta)} (\partial_x \theta - \frac{e^* d_1}{\hbar} B_{\text{ext}})$. In equilibrium, the relation $\partial_x \theta = 0$ holds in the bulk of the material, leading to a constant diamagnetic current $j_x = -\frac{c^2 \epsilon_0 \beta}{(1+\beta)} B_{\text{ext}}$. The resulting diamagnetic susceptibility, due to superconducting fluctuations, is given by $\chi_d = -\frac{\beta}{3}$, estimated from experimental data to be $\beta \sim 10^{-5}$, as described in the Methods (see also Appendix 2).

Near the edges of the sample, the in-plane component of the current goes to zero, being replaced by the Josephson current along the z -axis, as shown schematically in Fig. 1(b). The penetration depth of the diamagnetic screening current is given by $\lambda = \sqrt{\frac{\beta}{1+\beta} \frac{c}{\omega_J}}$. Rescaling the x coordinate by λ and the t coordinate by ω_J^{-1} , we

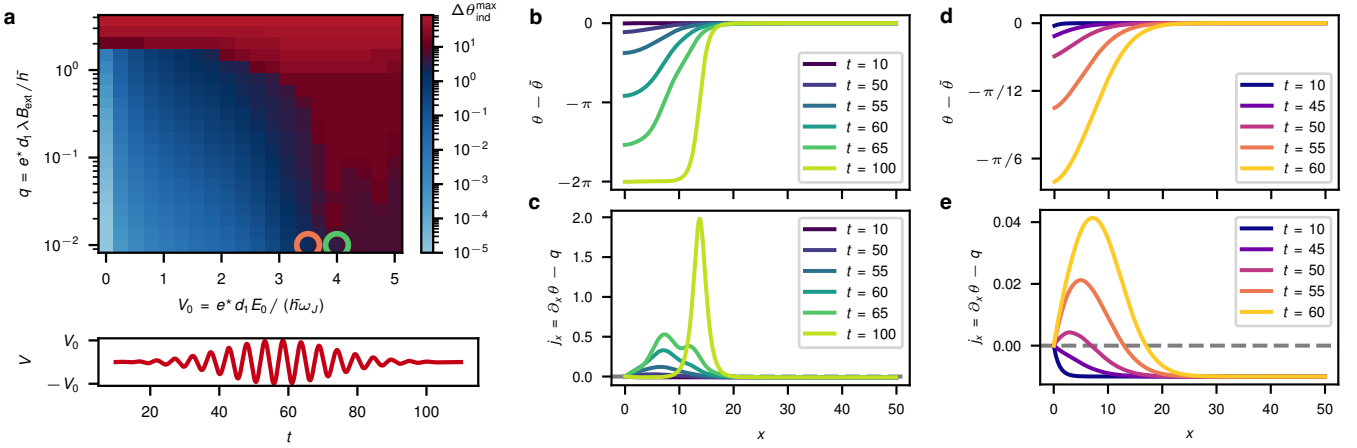


FIG. 2. Dynamical phase diagram of the driven SG model. **a** Heatmap of the maximum photo-induced phase difference across the entire segment, $\Delta\theta_{\text{ind}}^{\text{max}}$, in the (V_0, q) parameter space (upper plot) and time trace of the pump pulse with amplitude V_0 (lower plot). The Pokrovsky-Talapov transition is observed in the unpumped ($V_0 = 0$) limit for high enough magnetic field. For $V_0 > 0$, a rather sharp transition occurs between a soliton regime, marked by red, and a pre-soliton regime, marked by blue. **b** Snapshots of the phase and **c** snapshots of in-plane current for the combination $V_0 = 4$ and $q = 0.01$, representative of the soliton regime, corresponding to the point annotated with a green circle in panel (a). The small localized phase profile near the edge, present in equilibrium, monotonically grows upon driving until a full 2π soliton enters the system. We find a photo-induced sign change of the in-plane current. **d** Snapshots of the phase and **e** snapshots of in-plane current for the combination $V_0 = 3.5$ and $q = 0.01$, taken in the pre-soliton scenario, corresponding to the point annotated with an orange circle in panel (a). A boundary-localized feature, resembling a soliton but with much smaller amplitude, develops during pumping. This induces a sign change of the in-plane current. The following parameters are used in all plots: $L = 100$, $\alpha = 0.5$, and $\beta = 10^{-5}$. In both panels (b) and (d), the spatially uniform and fast oscillating component $\tilde{\theta}$ is subtracted off the phase θ . The dashed gray lines in both panels (c) and (e) indicate $j_x = 0$.

obtain the perturbed SG equation (and its BC) in dimensionless form:

$$\partial_t^2 \theta + \alpha \partial_t \theta - \partial_x^2 \theta + \sin \theta = \partial_t V, \quad (4)$$

$$\partial_x \theta|_{x=0,L} = q, \quad (5)$$

where we define the driving term $V(t) = V_0 e^{-\frac{(t-t_p)^2}{2\sigma^2}} \sin[\omega_p(t-t_0)]$ with amplitude $V_0 = \frac{e^* d_1 E_0}{\hbar \omega_J}$, the damping coefficient $\alpha = \frac{\sigma_n}{\epsilon_0 \omega_J}$ and the boundary field $q = \frac{e^* d_1 \lambda B_{\text{ext}}}{\hbar}$. Motivated by the experimental set-up³², we choose $\omega_p = 1.2$, $t_p = t_0 + 3\sigma$, $\sigma = 6\pi/\omega_p$ and $t_0 = 10$.

Photo-generated Josephson solitons. In Fig. 2(a), we plot the dynamical phase diagram of the driven SG model under a magnetic field, by numerically solving Eqs. (4) and (5). In particular, we compute the maximum photo-induced phase difference across a bilayer segment of length L , $\Delta\theta_{\text{ind}}^{\text{max}} = \max\{\theta|_{x=0}^{x=L} - \theta_{\text{eq}}|_{x=0}^{x=L}\}$ with $\theta_{\text{eq}} = \theta(x, t_0)$, as a function of the pump amplitude, V_0 , and magnetic field, q . Solitons in the SG model correspond to current loops known as Josephson vortices in the YBCO bilayer. The phase difference across a bilayer segment quantifies the net number of solitons injected inside the system, with $\Delta\theta_{\text{ind}}^{\text{max}} = 2\pi$ corresponding to one (net) soliton. In the unpumped limit, $V_0 = 0$, a well known transition exists for high enough magnetic field, called the *Pokrovsky-Talapov* transition^{49,50}, where solitons proliferate inside the segment. Our simulations show

that solitons can also be generated dynamically under strong driving, even in the presence of very small external magnetic field. The *soliton regime* is marked by red in Fig. 2(a), and we observe a relatively sharp transition line as a function of V_0 , which suggestss the onset of an instability beyond some critical pumping amplitude. In Fig. 2(b) and (c), the phase and in-plane current spatial profiles are plotted for different times during the drive, for a (V_0, q) pair representative of the soliton regime, see the green circle in Fig. 2(a). We observe that the small localized phase profile near the edge, present in equilibrium, monotonically grows upon driving until it becomes a full 2π soliton, which then enters the system. The typical phase and current profiles observed in the blue region of the phase diagram, i.e., where full solitons are not excited, are depicted in Fig. 2(d) and (e). We refer to this region as the *pre-soliton regime*, as the boundary-localized dynamical feature resembles a soliton but has a significantly smaller amplitude. We find that experiments³² are deep in the pre-soliton regime, with $V_0 \approx 3.5$ and $q \approx 10^{-4} - 10^{-5}$ such that $\theta(t=0) \ll 1$ and $\Delta\theta_{\text{ind}}^{\text{max}} \lesssim 0.1$. We note that, compared with j_x , θ and therefore the Josephson current j_z can be greatly enhanced relative to its initial value. The time dependent Josephson current serves as an antenna localized near the edge which drives an enhanced B field that decays into the bulk.

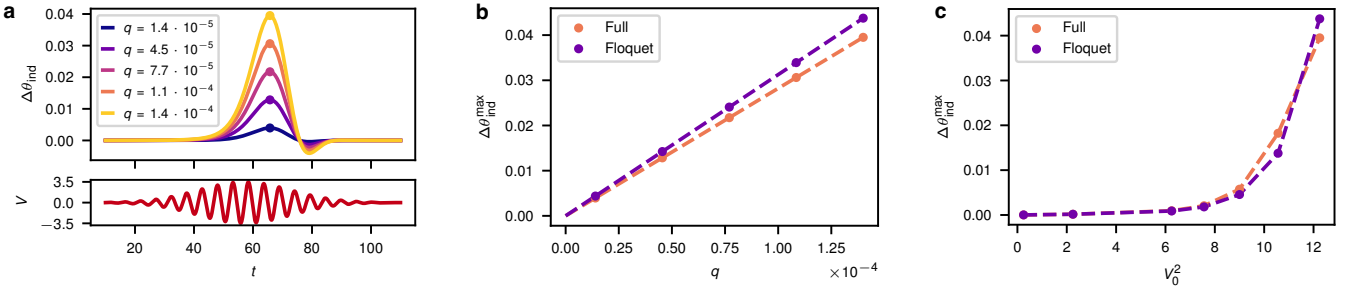


FIG. 3. Pre-soliton universality of the driven SG model. **a** Time traces of the photo-induced phase difference across the entire segment, for the full nonlinear model, at various external magnetic fields (upper plot) and the corresponding pump pulse (lower plot). Circles are used in the upper panel to denote the maxima of the different curves, all obtained for $V_0 = 3.5$. **b** Maximum photo-induced phase difference vs. the magnetic field, at $V_0 = 3.5$. The orange (purple) points are obtained by numerically solving the full nonlinear (Floquet effective) model. Despite the strongly nonlinear dynamics, the dependence on the external magnetic field is linear, and the two models show remarkable quantitative and qualitative agreement. **c** Maximum photo-induced phase difference as a function of fluence, V_0^2 , at $q = 1.4 \times 10^{-4}$. The orange points result from numerical integration of the full nonlinear model, while purple points correspond to the effective Floquet model. An initial linear increase for small fluences is then followed by an exponential increase beyond a critical amplitude. The two models are in clear quantitative and qualitative agreement here as well. The following parameters are used in all plots: $L = 100$, $\alpha = 0.5$, and $\beta = 10^{-5}$.

In Fig. 3(a), we plot the $\Delta\theta_{\text{ind}} = \theta|_{x=0}^{x=L} - \theta_{\text{eq}}|_{x=0}^{x=L}$ profiles as function of time, for several values of q in the experimental range, at $V_0 = 3.5$. We find that $\Delta\theta_{\text{ind}}$ is positive and increases during pumping, before returning back to equilibrium after the pump pulse is gone. The full solution of Eqs. (4) and (5) shows a linear dependence of $\Delta\theta_{\text{ind}}^{\text{max}}$ vs. q in the pre-soliton regime, for fixed V_0 , see the orange points in Fig. 3(b). The orange curve in Fig. 3(c) illustrates the behavior of $\Delta\theta_{\text{ind}}^{\text{max}}$ with respect to pump fluence, V_0^2 , for fixed q . Here we observe a linear increase, similar to an inverse Faraday effect⁵¹, for small fluences $V_0^2 < 10$. Beyond a critical value of $V_0^2 \approx 10$, we find an exponential growth of the maximal photo-induced phase difference.

Floquet effective model for the pre-soliton regime. To better understand the physics of the pre-soliton regime, we decompose the solution of our nonlinear problem into two parts: $\theta(x, t) = \tilde{\theta}(t) + \theta'(x, t)$, where $\tilde{\theta}(t)$ obeys the driven damped pendulum equation of motion

$$\partial_t^2 \tilde{\theta} + \alpha \partial_t \tilde{\theta} + \sin \tilde{\theta} = \partial_t V(t), \quad (6)$$

with BC $\partial_x \tilde{\theta}|_{x=0, L} = 0$, and $\theta'(x, t)$ satisfies the BC given by Eq. (5). In the small q limit relevant for the pre-soliton regime, the condition $\theta' \ll 1$ holds even if the pump is strongly nonlinear and $\tilde{\theta}$ is not small. In this case, we can expand the nonlinear term in Eq. (4) as $\sin \theta \approx \theta' \cos \tilde{\theta}$. We begin by factorizing this product and replace $\cos \tilde{\theta}$ by $\langle \cos \tilde{\theta} \rangle$, its average over several cycles at the pump frequency. We obtain the following *linear* equation, where the drive is encoded in a modified restoring force η , subject to the same BC

$$\partial_t^2 \theta' + \alpha \partial_t \theta' - \partial_x^2 \theta' + \eta \theta' = 0, \quad (7)$$

$$\partial_x \theta'|_{x=0, L} = q. \quad (8)$$

By approximating $\tilde{\theta} \approx A \sin(\omega_p t)$, where $A(t)$ is a slow-varying envelope, we find that $\eta(A) \approx \langle \cos[A \sin(\omega_p t)] \rangle \approx J_0(A)$ where J_0 is the Bessel function. Importantly, this average can be negative since J_0 can reach a minimum value of ~ -0.4 . Thus the oscillator in Eq. (7) can be in the unstable regime, resulting in the amplification found in the exact solution. It is clear that the average $\langle \cos[A \sin(\omega_p t)] \rangle$ does not depend on the phase of the drive, which we have set to be zero. Therefore, the sign of the effect does not depend on the phase of the drive, which is in agreement with our exact numerical solution. In the Methods (see also Appendix 3), we derive a more accurate expression for $\eta(A)$ using a Floquet expansion.

Remarkably, there is very close agreement between the full nonlinear solution and that of the Floquet effective model shown by the purple points in both Fig. 3(b) and (c). The effective model gives us an intuitive way to understand the numerical results: even though the homogeneous oscillations caused by the drive are very large, the effective dynamics for θ' are linear to a very good approximation, since q is small. Due to this linearity, the photo-induced response is proportional to q . On the other hand, for sufficiently large amplitudes V_0 , $\eta(A)$ in Eq. (7) becomes negative, thereby triggering an instability and exponential growth of θ' .

In the Methods, we repeat the SG calculations in the presence of a soliton or an antisoliton in the initial conditions. Our results indicate that, as long as these excitations are located more than a few penetration depths ($\lambda < 100$ nm) away from the bilayer segment's edges, the discovered mechanism is not affected by their presence. More generally, we argue that our results remain robust in the presence of thermal fluctuations $\theta(x, y, t)$ and is

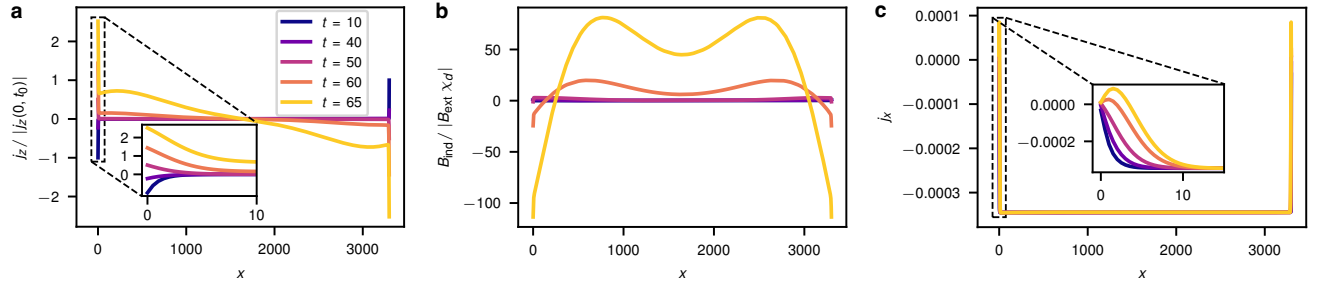


FIG. 4. Photo-induced instability in a multi-bilayer segment. **a** Snapshots of the effective current along the z -direction, j_z , in units of its magnitude at $x = 0$ before pumping, $|j_z(0, t_0)|$. The inset plot zooms on the $0 \leq x \leq 10$ region. When reaching the unstable regime in the presence of strong enough driving, j_z can change sign and become paramagnetic even though $|\theta'|$ monotonically increases. **b** Snapshots of the average magnetic field induced within a unit cell, B_{ind} , normalized by the equilibrium diamagnetic field amplitude, $|B_{\text{ext}} \chi_d|$. The field originates from edge currents, and it propagates from the system's boundaries inwards at the speed of light in the YBCO crystal. **c** Snapshots of the dimensionless in-plane current j_x , showing a dynamical behavior analogous to that highlighted for the pre-soliton currents in a single bilayer shown in Fig. 2(e). The inset zooms in to the $0 \leq x \leq 15$ region. All three plots are obtained using the Floquet effective model extended to multilayers (see Methods), for the following realistic (normalized) parameter set: $L = 3300$, $V_0 = 3.5$, $q = 2.3 \times 10^{-4}$, $|\chi_d| = 10^{-5}$, $\alpha_1 = 0.4$, $\alpha_2 = 6$, which denote damping in the intra- and inter-bilayer regions (see Methods). The legend in panel (a) applies to panels (b) and (c) as well, where time is rescaled to $1/\omega_J$.

applicable up to the pseudogap temperature T^* . Due to the Josephson energy, which acts as an external field in the XY model, there will be patches where the equilibrium θ is pinned to the vicinity of multiples of 2π . If the correlation length in these patches is longer than the penetration depth λ , a 2D version of the scaled Eq. (4) will hold. Assuming the fluctuations evolve slower than the pump duration, we can take a snapshot as initial conditions for θ and do a similar decomposition into $\tilde{\theta}$ and θ' . For small q , θ' satisfies Eqs. (7) and (8), with η given by $\langle \cos \tilde{\theta}(x, y, t) \rangle$. Upon temporal and space average, the sensitivity to initial condition will average out, and η can still become negative, leading to exponential growth of θ' and a similar phenomenology to the one described in this section.

Our results show a significant dependence on the dissipation coefficient, α . Since the large enhancement of $\Delta\theta_{\text{ind}}^{\text{max}}$ is triggered by an instability, α directly impacts the magnitude of the effect by modifying its growth rate. In Appendix 4, we illustrate this dependence by presenting simulations for different values of α . Interestingly, while small α leads to a large enhancement of the effect, in the limit of too small of a dissipation, the emergence of oscillatory modes such as low-amplitude breathers^{38,39} can complicate the simple picture presented above, leading to a more oscillatory behaviour in the $\Delta\theta_{\text{ind}}$.

For completeness, in Appendix 4, we present a number of space-time contour plots for the evolution of the phase and its gradient, θ and $\partial_x \theta$, together with animations of the same numerical runs, to further illustrate the strongly nonlinear dynamics discussed here.

4. PUMPED MULTI-BILAYER PSEUDOOGAP YBCO

In this section, we present results for the pumped multi-bilayer case. Although the Josephson coupling between the bilayers is zero, they remain capacitively coupled through Maxwell equations. We simulate the dynamics in a finite segment in the x direction, with radiative BC, see the Methods for a detailed account of the equations of motion. This allows to track both the induced magnetic field inside a finite pumped YBCO strip, as well as the emitted radiation outside of the strip. In the Appendix 5, we further explore the dependence on dissipation.

Photo-excited edge currents in the multi-bilayer system. At the microscopic level, we attribute the origin of the photo-induced giant paramagnetism to the instability of the SG model discussed above. More specifically, within our Floquet effective theory, we established that the magnitude of the phase inside the bilayer, $|\theta'|$, exponentially grows when $\eta(A) < 0$. At the same time, the effective current along the z -direction is given by $j_z = \eta(A) J_c \sin \theta'$, which changes sign and become paramagnetic when $\eta < 0$, as shown in Fig. 4(a), even though $|\theta'|$ monotonically increases during pumping. The latter current creates a displacement current of similar magnitude across different bilayers due their capacitive and resistive coupling. This leads to paramagnetic edge currents, with opposite signs at the two edges. Remarkably, the key difference between the multi-bilayer and the single bilayer is that the space between bilayers now acts as a wave-guide, so that the displacement current and the magnetic field it produces propagate into the bulk

at the speed of light in the YBCO crystal from the system's boundaries inwards, see Fig. 1(d) and Fig. 4(b). In Fig. 4(c), we show the corresponding in-plane current j_x , whose dynamical structure is consistent with that of the pre-soliton currents identified previously for a single bilayer.

Even though the current at the edge is similar in magnitude with the single bilayer case, the upshot is that the magnetic field extends into the bulk, therefore greatly increasing the flux that is generated. This mechanism is crucial for us to obtain a large enough effect to compare with experiment. Using realistic parameters, the induced field averaged inside and between bilayers, $B_{\text{ind}}(x)$, becomes $O(100)$ -times larger than the equilibrium diamagnetic field amplitude, $|B_{\text{ext}}\chi_d|$. This is shown in Fig. 5(a). We also show that the magnitude of the induced magnetic field scales linearly with the equilibrium diamagnetic susceptibility $|\chi_d|$ over more than an order of magnitude, see Fig. 5(b). Since χ_d is proportional to the local superfluid density n_s , it is expected to go to zero in a BCS way near $T^* \approx T_{MF}$ as sketched in the inset. The induced magnetic field amplitude is expected to show this temperature dependence, in agreement with experiment. The traveling-wave character of our mechanism also results in a peculiar segment-size dependence that is addressed in the Appendix 5. For completeness, in our simulations, we also track the magnetic fields emitted outside the pumped region in the infinite strip geometry, which we discuss in the Methods. In general, due to flux conservation, any short-lived response in pumped YBCO with a definite sign, either diamagnetic or paramagnetic, will result in a bimodal emission pattern in the far-field, carrying both positive and negative signs, averaging to zero in time. In order to make connection with experiment, it is necessary to modify this geometry to take into account the presence of a mask blocking the pump for $z > 0$. This will be discussed in the next section.

5. RELATION TO EXPERIMENTS

In the experiment, a mask is placed over the magnetic field detector to protect it from the high intensity pump field. The edge of the mask is parallel to the long axes of the bilayer [x-axis in Fig. 6(a)] and covers the area $z > 0$. This geometry is different from what is considered in the last section, where the YBCO is an infinitely long strip running along z . The important difference is that now the radiation generated by the edge current can escape into the $z > 0$ region and reach the detector. As mentioned earlier, the sample is broken up into domains separated by cracks and defects. The typical domain size is roughly 10 μm . A transient current is generated at the edge of each domain, as sketched by the red arrows in Fig. 6(a). Each domain constructively contributes to the emitted radiation in the $z > 0$ area and we expect the net result

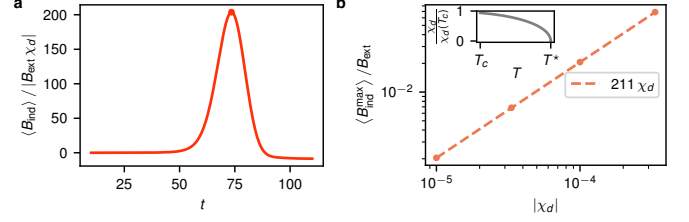


FIG. 5. **Time dependent induced magnetic field under strong pumping**. **a** Average induced magnetic field, $\langle B_{\text{ind}} \rangle$, normalized by the equilibrium diamagnetic field amplitude, $|B_{\text{ext}}\chi_d|$, as a function of time. Here the symbol $\langle \dots \rangle$ indicates averaging over a segment of length L . The obtained peak magnetic response is $\chi_{\text{ind}} \sim -100\chi_d$, see the circle. The parameter values for this numerical run are given in Fig. 4. **b** Dependence of the (normalized) peak magnetic response, $\langle B_{\text{ind}}^{\text{max}} \rangle / B_{\text{ext}}$, versus the equilibrium susceptibility χ_d , showing proportionality. Since χ_d is proportional to the local superfluid density n_s , which goes to zero in a BCS way near $T^* \approx T_{MF}$ as sketched in the inset, we expect the signal to decrease to zero near T^* , in agreement with experiment. Here we choose $L = 18c/\omega_J$, $B_{\text{ext}} = 10\text{ mT}$, $V_0 = 3.5$, $\alpha_1 = 0.4$, and $\alpha_2 = 6$.

to be similar to that of a single domain with the size of the spot, but we have not pursued detailed modeling of this correspondence.

As a test case, we consider two domains spanning a total length of 100 μm , corresponding to the spot size. We investigate the emitted magnetic field distribution in the shielded region ($z > 0$) due to time-dependent 2D edge currents with a Gaussian time profile of duration ~ 2 ps (centered at $t = 0$). For simplicity, the layers are assumed to be infinite along y , ensuring translation invariance in that direction. A time-dependent sheet of current flows along z at the domain edges, extending from $z = 0$ to $-z_{\text{spot}}$ and remaining uniform along y . The masked region ($z > 0$) is modeled as an insulator with refractive index $n = 3$, a value consistent with experimental observations³². We fit the amplitude of the edge currents to match the overall magnetic field amplitude predicted in the previous section, and then solve Maxwell's equations for the space- and time-dependent magnetic field under the shielded region where the detector is placed, see Appendix 6.

Snapshots of the magnetic field distribution beneath the mask are shown at $t = 0, 1, 1.5$ ps, respectively, in Fig. 6(a), (b), (c). Furthermore, an animation of the propagation of the magnetic field under the mask can be found in Ref. 52. A propagating front $O(100)$ -times larger than the equilibrium diamagnetic field amplitude, $|B_{\text{ext}}\chi_d|$, is seen to reach the detector area. To further illustrate our point, we take an observation coordinate $x = 40\text{ }\mu\text{m}$ (measured from the leftmost segment edge) and the following separations along z from the pumped region: $\Delta z = 50\text{ }\mu\text{m}$, $\Delta z = 100\text{ }\mu\text{m}$, and $\Delta z = 150\text{ }\mu\text{m}$

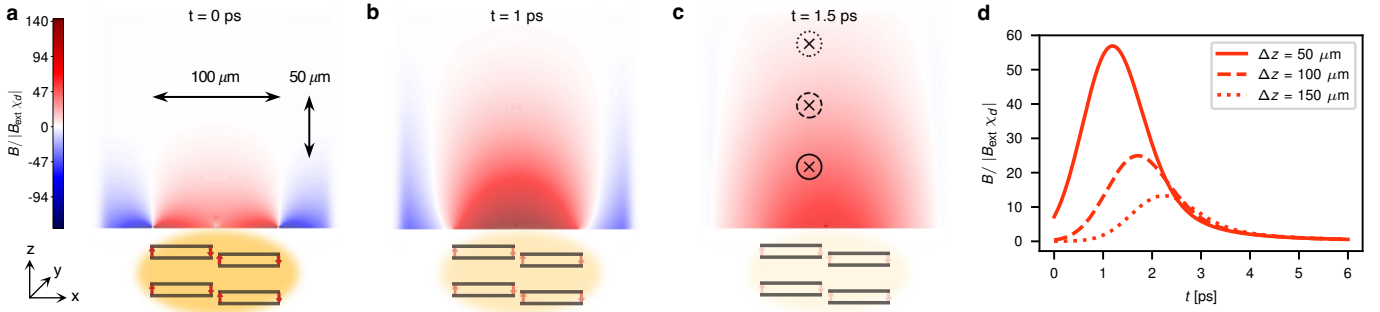


FIG. 6. Electromagnetic wave propagating from the pumped region. Geometry of the detection method in experiments. A mask is used to protect the magnetic field detector from the pump pulse that covers the area $z > 0$. This area is shown in panels (a), (b), and (c). Illuminated defects and edges will give rise to a paramagnetic signal, propagating at the speed of light in the material and reaching the region underneath the detector. To illustrate this, we report snapshots of the magnetic field distribution beneath the mask at time **a** $t = 0$ ps, **b** $t = 1$ ps, and **c** $t = 1.5$ ps. The axes, physical scales, and colorbar from panel (a) apply to panels (b) and (c) as well. This calculation is performed on a two-segment system, pumped over $100 \mu\text{m}$ along the z direction. We also assume a Gaussian-like induced response centered at $t = 0$ and extending in time over 2 ps . **d** Magnetic field profile B versus time at three selected locations: $\Delta z = 50 \mu\text{m}$, solid line; $\Delta z = 100 \mu\text{m}$, dashed line; $\Delta z = 150 \mu\text{m}$, dotted line. This calculation is produced for the observation coordinate $x = 40 \mu\text{m}$, see panel (c) for a sketch, under the same geometry and induced response of the previous panels. Throughout the figure, the magnetic field B is scaled by the equilibrium diamagnetic field amplitude.

(corresponding, respectively, to the full, dashed, and dotted circles in Fig. 6(c)). At these locations, we show in Fig. 6(d) the time traces of the induced magnetic field. In agreement with experiment, we observe a pulse propagating along z at the speed of light in the medium and progressively attenuating in strength.

To summarize, we now present a detailed comparison between the experimental observations of Ref. 32 and the predictions made within our theoretical framework:

a. The peak magnetic field on the detector is paramagnetic and linear with applied external magnetic field. This is recovered by our theory. As discussed above, even though experimental parameters are deep in the non-linear dynamical regime of the SG model, the response scales linearly with the magnetic field, see Fig. 3(b);

b. The induced magnetization measurements show a highly nonlinear behavior versus fluence, with a saturation trend at the highest fluences. We capture the fluence response seen in experiments for low fluences, see Fig. 3(c). For higher fluences, we do not observe the reported saturation. To explain the saturating behavior, we point to the sensitive dependence of the phenomenon to dissipation demonstrated in Appendix 4. A heavy increase of dissipation, due to heating at such higher fluences, could indeed account for the observed saturation;

c. The magnetic pulse on the detector is paramagnetic and travels with the speed of light. We calculate the magnetic field distribution beneath the mask shielding the magnetic field detector, assuming the geometry and edge-current distribution illustrated in Fig. 6(a). The medium beyond the mask's edge is modeled, at THz frequencies, using an effective dielectric constant matching with experimental observations³². This approach attributes the response observed in Ref. 32 to giant dynamical param-

agnetism propagating through the region under the detector. As shown in Fig. 6(d), increasing the propagation distance causes the signal to attenuate and shift to longer delays, consistent with the measurements in Ref. 32 and the behavior of a propagating electromagnetic wave.

d. The amplitude of the induced magnetic field is $B_{\text{ind}} \approx 6 \mu\text{T}$ for an external field of $B_{\text{ext}} \approx 10 \text{ mT}$. Using realistic parameters, we obtain a result which quantitatively agrees with the experiment, $B_{\text{ind}}/B_{\text{ext}} \sim 10^{-3}$, see Fig. 5(a). The intra-bilayer effective conductivity σ_n , which determines the damping coefficient as $\alpha = \frac{\sigma_n}{\epsilon_0 \omega_J}$, is hard to determine either from first principles or experimentally. Reducing (increasing) the latter parameter greatly enhances (attenuates) the effect;

e. Temperature dependence of the effect. While various parameters, such as ω_J and α , can in principle contribute to the temperature dependence of the overall result for B_{ind} , we start by focusing on the direct proportionality to the equilibrium diamagnetic field shown in Fig. 5(b): $\langle B_{\text{ind}}^{\text{max}}(T) \rangle / B_{\text{ext}} = -f(T) \chi_d(T)$, where $\langle \dots \rangle$ indicates averaging over a segment of length L . The equilibrium diamagnetic response, χ_d , is proportional to the local superfluid density, i.e., $\chi_d \propto n_{2D,s}(T)$. Assuming a preformed pair scenario, the critical temperature, T_c , is associated with a BKT transition, whereas the pseudo-gap temperature, T^* , is interpreted as that where Cooper pairs dissociate, thereby depleting the superfluid density. In the inset of Fig. 5(b), we plot the temperature dependence of χ_d , assuming a BCS form for the superfluid density: $n_s(T)/n_s(T_c) = \tanh\left(\sqrt{\kappa \frac{T^* - T}{T}}\right)$. The fact that the photo-induced effect, which is proportional to χ_d , can be fitted using this expression, as shown in the experimental paper³², is highly suggestive for the nature of

the pseudogap phase.

We emphasize that our mechanism is very different from that proposed in Ref. 32, where the paramagnetic signal is interpreted as originating from flux exclusion from a giant diamagnetic response under the pump. This mechanism can be distinguished from ours in future experiments that measure the magnetic field directly under the pumped regions, since opposite signs are predicted⁵³. A second proposal is to place the mask so that it runs perpendicular to the layer orientation, instead of parallel as in Ref. 32. This geometry is close to that treated in Sec. 4, if we interpret the sample between 0 and L as the pumped region and the area under the mask as the region outside one edge of the sample. In this case, we expect the emitted magnetic flux to be bimodal and mostly canceled upon a short time integration, as seen in Fig. 7, implying a much smaller observed magnetic field.

DISCUSSION

It is useful to position our work in the general landscape of ultrafast probes of electron states and photo-induced phases. A ubiquitous challenge in this field is identifying the correct methodology for analyzing experimentally measured properties of transient states. A common approach is to use the quasi-static perspective, in which experimental signatures are interpreted in direct analogy with equilibrium systems. This approach demonstrably breaks down when transient regimes feature qualitatively different properties from the static systems. In these cases, one needs to take into account the dynamical character of photoinduced states. Notable examples include light induced renormalization of electronic bands, which can lead to Floquet topological systems^{54,55} or changes in terahertz optical properties due to photoexcited collective modes, that result in new features in reflectivity and even light amplification^{18,56–58} (for related studies, see also analysis of photonic time crystals⁵⁹). The theoretical analysis presented in this paper suggests that experimental results of the Hamburg group³² should be interpreted from this dynamical perspective rather than by analogy with the equilibrium Meissner effect. We point out that in the case of bilayer YBCO, there is a large separation in Josephson coupling strengths within bilayers and between them. This gives rise to an extended temperature range, in which bulk diamagnetic response is suppressed because there can be no static flow of screening currents between the bilayers; however, charge dynamics within bilayers is dominated by preformed Cooper pairs. Thus, we argue that experimentally observed light induced giant paramagnetic effect in YBCO is a result of the dynamical instability of strongly driven Josephson plasmons within individual bilayers in the presence of static magnetic field. We demonstrate that this phenomenon reveals itself in the macro-

scopic properties of the system, because at finite frequencies Maxwell's displacement currents can supplant the charge currents. The phenomenon of giant paramagnetic response triggered by dynamic instability has no static analogues. Our work demonstrates that in layered superconductors above T_c , short-range superconducting correlations can be revealed in the far out of equilibrium dynamics, even when the canonical linear response probes, such as diamagnetic susceptibility, do not provide indications of enhanced pairing fluctuations. Hence, the photomagnetic phenomena observed in Hamburg experiments provide another demonstration of the importance dynamical aspects of photoinduced transient states in ultrafast experiments in solids.

In regards to the physics of the pseudogap phase, the phenomena uncovered in this paper crucially depend on the existence of local pairing correlations. While evidence for such correlations has been reported up to a temperature of 180 K^{60,61}, the same cannot be stated up to $T^* \approx 300 - 400$ K. If our interpretation is correct, the magnetic field response observed in experiments³² would represent the first evidence of local superconducting correlations surviving up to the pseudogap temperature T^* . This point of view will be further supported in a separate paper⁶², which shows that the same model can explain the optical response and second harmonic generation experiments^{18,19}. The origin of the pseudogap has been under debate for decades. Much of the discussions has centered on anti-ferromagnetic spin fluctuations, identifying the gap as a spin gap due to some underlying resonating valence bond (RVB) scenario⁶³, or suppression of spectral weight due to strong correlation near the Mott transition⁶⁴. Occasionally, pairing scenarios such as pair density waves have also been proposed^{65,66}. We note that recent low-temperature local shot noise measurements with scanning tunneling microscopy (STM) have been used to infer that the large pseudogap is a pairing gap⁶⁷, which aligns with the picture presented in this paper. The notion of local pairing surviving up to T^* will clearly have a strong impact towards resolving the pseudogap puzzle.

Before concluding this paper, we point out that the instability discussed here can be utilized to achieve the amplification of magnetic field in systems based on extended Josephson junctions⁶⁸.

METHODS

Electrodynamics of the counterflow pseudogap state. In the pseudogap, there is no long-range superconducting coherence, so both the in-plane and out-of-plane DC currents are dissipative due to the proliferation of vortices. However, strong Josephson coupling within a single bilayer leads to locking of vortex lines passing through it. This gives rise to intrabilayer supercon-

ducting coherence⁴⁶ and dissipationless in-plane currents flowing in opposite directions⁴⁸. The minimal model capturing these basic ingredients can be formulated as follows for the currents:

$$\partial_t j_{z,1} = \frac{e^* d_1}{\hbar} J_{c,1} E_{z,1} \cos \theta_1, \quad (9)$$

$$\partial_t j_{x,1} = \frac{(e^*)^2 n_s}{m} E_{x,1} + \gamma_d (j_{x,1} + j_{x,2}), \quad (10)$$

$$\partial_t j_{x,2} = \frac{(e^*)^2 n_s}{m} E_{x,2} + \gamma_d (j_{x,1} + j_{x,2}), \quad (11)$$

for a generic unit cell, where the label ‘ $z, 1$ ’ (‘ $z, 2$ ’) denotes the average of a z -component between layers separated by a distance d_1 (d_2), and ‘ $x, 1$ ’ (‘ $x, 2$ ’) an x -component evaluated at the $z = z_1$ ($z = z_2$) layer. Within the bilayer, the superconducting coherence is encoded in the Josephson relation. We assume interbilayer coherence to be completely lost, in accordance with the

experimental and numerical observation of the lower Josephson plasmon’s disappearance at $T = T_c$ in YBCO. Furthermore, the total in-plane current, $j_{x,1} + j_{x,2}$, is dissipative due to vortex motion⁶⁹ (γ_d is the corresponding friction coefficient), while the counterflow current, $j_{x,1} - j_{x,2}$, remains dissipationless. This assumption can be relaxed by adopting a two-fluid model, where a normal component is added to the counter-flow current. This replaces $(e^*)^2 n_s / m$ by $(e^*)^2 n_s / m + i\omega\sigma_{2D}$ and introduces an imaginary part to the parameter β , where σ_{2D} is the in-plane 2D normal conductivity. As a result, an extra dissipative term of the form $\partial_t \partial_{xx}$ is added to the equation below. We find that this term has very little effect on the results, due to the extra x derivatives.

As we describe in Appendix 1, combining Eqs. (9)–(11) with a normal-fluid dissipative current contribution and Maxwell’s equations leads to the following effective electrodynamic equations for the momentum $q_z = 0$ response in the pseudogap phase:

$$\partial_t^2 \theta_1 + \frac{\sigma_{n,1}}{\epsilon_0} \partial_t \theta_1 - \frac{c^2 (d_1 + d_2 \beta)}{d_1 + d_2 (1 + \beta)} \partial_x^2 \theta_1 + \omega_{J,1}^2 \sin \theta_1 = \frac{e^* d_1}{\hbar} \partial_t E_p(t) + \frac{c^2 d_1}{d_1 + d_2 (1 + \beta)} \partial_x^2 \theta_2, \quad (12)$$

$$\partial_t^2 \theta_2 + \frac{\sigma_{n,2}}{\epsilon_0} \partial_t \theta_2 - \frac{c^2 d_2 (1 + \beta)}{d_1 + d_2 (1 + \beta)} \partial_x^2 \theta_2 = \frac{e^* d_2}{\hbar} \partial_t E_p(t) + \frac{c^2 d_2}{d_1 + d_2 (1 + \beta)} \partial_x^2 \theta_1, \quad (13)$$

which describe a set of capacitively coupled long Josephson junctions. Here $\sigma_{n,1}$ denotes the normal c-axis conductivity between members of the bilayer and leads to dissipation. Formally, we introduce a similar quantity $\sigma_{n,2}$ in Eq. (13) to describe dissipation of θ_2 . However, due to the weak tunnel coupling between bilayers, the actual normal conductivity is negligible. The $\sigma_{n,2}$ originates from the fact that the cavity for the radiation field formed by the region between bilayers is leaky. The cavity Q leads to dissipation of photon modes, which can be parameterized by $\sigma_{n,2}$. Similar to the single bilayer case, we introduce the dimensionless intra-bilayer and interbilayer damping coefficients $\alpha_1 = \frac{\sigma_{n,1}}{\epsilon_0 \omega_{J,1}}$ and $\alpha_2 = \frac{\sigma_{n,2}}{\epsilon_0 \omega_{J,1}}$, respectively. Since α_1 and α_2 have different physical origins, they can take on very different values, as chosen in Fig. 4 in the main text. The main approximation made here is to work with averaged quantities between different layers. We note in passing that the perturbed SG model, see Eq. (1) in the main text, is readily recovered in the $d_2 \rightarrow \infty$ (single bilayer) limit of Eq. (12).

As shown in Appendix 1, the gauge invariant phase differences between layers, θ_1 and θ_2 , can be directly related to the average out-of-plane electric fields, $E_{z,1}$ and

$E_{z,2}$:

$$\partial_t \theta_1 = \frac{e^* d_1}{\hbar} E_{z,1}, \quad (14)$$

$$\partial_t \theta_2 = \frac{e^* d_2}{\hbar} E_{z,2}. \quad (15)$$

By relating the discontinuity of B across each layer to the in-plane currents, simple expressions for θ_1 and θ_2 in terms of the average in-plane magnetic fields between layers, $B_{y,1}$ and $B_{y,2}$, also hold:

$$\partial_x \theta_1 = \frac{e^* d_1}{\hbar} \left(B_{y,1} + \frac{B_{y,1} - B_{y,2}}{\beta} \right), \quad (16)$$

$$\partial_x \theta_2 = \frac{e^* d_2}{\hbar} \left(B_{y,2} + \frac{B_{y,2} - B_{y,1}}{\frac{d_2}{d_1} \beta} \right). \quad (17)$$

For earlier theoretical studies of Josephson plasmons in layered superconductors below T_c , see Refs. 70–76.

Diamagnetism due to the dissipationless counterflow state. To find the static response to an external magnetic field B_{ext} , we consider a semi-infinite geometry with a boundary to air at $x = 0$, and impose the BC: $B_{y,1}|_{x=0} = B_{y,2}|_{x=0} = B_{\text{ext}}$. In Appendix 2, the solu-

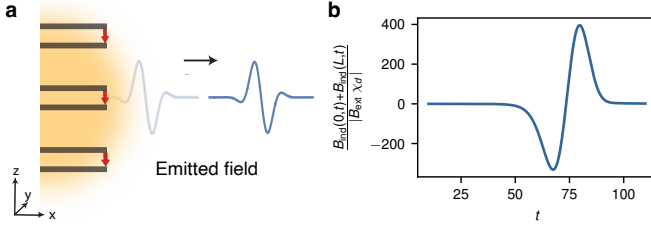


FIG. 7. **Magnetic field emitted from pumped YBCO.** **a** Sketch of the magnetic pulse emitted from the right edge ($x > L$) of a YBCO region illuminated by the pump field. An analogous emission process occurs at the left edge ($x < 0$) of the segment (not shown). **b** Average induced magnetic field at the edges, $B_{\text{ind}}(0, t) + B_{\text{ind}}(L, t)$, normalized by the equilibrium diamagnetic field amplitude, $|B_{\text{ext}}\chi_d|$. We observe a bimodal emission profile. The chosen simulation parameters are identical to that of Fig. 4, see the main text, and time is rescaled to $1/\omega_{J,1}$.

tion of Eqs. (12)–(13) is shown to be

$$B_{y,1}(x) = \left(\frac{\beta}{1+\beta} e^{-x/\lambda} + \frac{1}{1+\beta} \right) B_{\text{ext}}, \quad (18)$$

$$B_{y,2}(x) = B_{\text{ext}}, \quad (19)$$

where $\lambda = \sqrt{\frac{\beta}{1+\beta}} \frac{c}{\omega_J}$ is the bilayer penetration depth. For $x \gg \lambda$, we find a screened intrabilayer magnetic field, $B_{\text{sc}} = \frac{B_{\text{ext}}}{1+\beta}$, whereas there is no interbilayer screening. Averaged over one unit cell, the effective diamagnetic susceptibility is given by:

$$\chi_d = -\frac{d_1\beta}{D} = -\frac{d_1(e^*)^2 n_s}{D 2\epsilon_0 m c^2}, \quad (20)$$

where, in the second step, we expressed β in terms of microscopic parameters of the counterflow state, such as the 2D superfluid density, n_s , in each layer.

From existing data in the pseudogap phase of YBCO⁴³, a geometric analysis of magnetic susceptibility found an enhanced diamagnetic contribution for the in-plane susceptibility, which is sensitive to counterflow currents, versus the out-of-plane magnetic susceptibility, with $\delta\chi \sim 10^{-5}$. Attributing this difference to the counterflow state, we estimate $\beta \sim 10^{-5}$.

Radiative BC. Focusing on the physics between two cracks, BC are required to model the electrodynamics outside the pumped segment. Specifically, as localized paramagnetic currents are generated and amplified in the pre-soliton regime, an equal and opposite flux is expected to be emitted from the segment's edges, such that the total flux is conserved. By imposing appropriate continuity conditions for the average electric and magnetic fields at the segment-to-exterior interface, as illustrated

in Appendix 1, we obtain:

$$\left[\partial_x \theta'_1 + \partial_x \theta'_2 \mp \frac{1}{c} (\partial_t \theta'_1 + \partial_t \theta'_2) \right] \Big|_{x=0,L} = \frac{e^* D}{\hbar} B_{\text{ext}}, \quad (21)$$

$$\left(\frac{\partial_x \theta'_1}{d_1} - \frac{\partial_x \theta'_2}{d_2} \right) \Big|_{x=0,L} = 0, \quad (22)$$

where the $-$ ($+$) sign applies to the $x = 0$ ($x = L$) boundary. As motivated above, we decomposed our dynamics as $\theta_{1,2}(x, t) = \tilde{\theta}_{1,2}(t) + \theta'_{1,2}(x, t)$, with $\tilde{\theta}_{1,2}$ being the homogeneous parts, strongly driven and evolving over the pump period's timescale, and $\theta'_{1,2}$ mostly keeping track of slower (over the pump envelope's timescale) and spatially localized features.

In the segment's exterior, concentrating on the right-propagating mode sketched in Fig. 7(a), we then have that

$$B_{\text{em}}(x > L, t) = B_{\text{ind}}(L, t - (x - L)/c), \quad (23)$$

where $B_{\text{ind}} = \frac{\hbar}{e^* D} (\partial_x \theta'_{1,\text{ind}} + \partial_x \theta'_{2,\text{ind}})$ is the z -averaged field induced within a unit cell. Taking also into account the left-propagating mode for $x < 0$, total flux conservation readily implies that

$$B_{\text{ind}}(0, t) + B_{\text{ind}}(L, t) = -\frac{1}{cD} \partial_t \Phi_{\text{ind}}, \quad (24)$$

with Φ_{ind} being the induced flux inside the segment. Therefore, the information about the emitted fields is encoded in the $B_{\text{ind}}(0, t) + B_{\text{ind}}(L, t)$ time traces, shown in Fig. 7(b) for our representative multi-bilayer scenario. The emission profile is bimodal, which can be understood as a consequence of flux conservation. To conserve total flux, as the induced flux in the segment increases, a diamagnetic pulse is emitted outward from the segment. Conversely, when the induced flux decreases, a paramagnetic flux is emitted. In general, we expect any short-lived paramagnetic or diamagnetic response to give rise to a bimodal emission, which averages to zero over time, in accordance with Eq. (24).

SG pre-soliton mechanism: length dependence and robustness to thermal (anti)solitons. Being a spatially extended excitation, a pre-soliton can only form if the bilayer system is large enough to host it. To this end, we explore the SG model's ($\theta_1 \equiv \theta$ here) response versus the (normalized) inverse segment length $0.01 \leq L^{-1} \leq 1$, see Fig. 8(a). We observe a saturating behavior, with a characteristic inverse length of ~ 0.1 , which is consistent with the pre-soliton size of ~ 20 we deduce from, e.g., Fig. 2(d) and (e). The latter point confirms, at the SG level, that this is indeed a boundary effect.

We have not explicitly studied the influence of thermally excited solitons and antisolitons on our mechanism. For $T \gtrsim T_c$, our choice is justified because the density of such fluctuations is presumably very small by

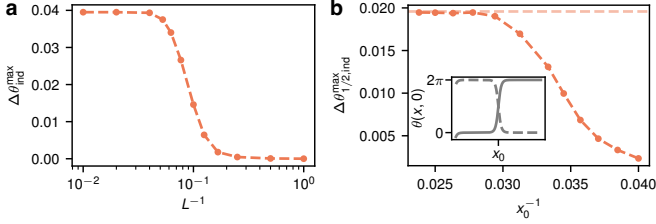


FIG. 8. **Size analysis and impact of solitonic initial conditions.** **a** Dependence of the maximum photo-induced phase difference versus the (normalized) inverse length of the bilayer segment. If $L < 10$, i.e., if the segment is smaller than the characteristic length of the pre-soliton shown in Fig. 2, the effect is heavily suppressed, whereas for $L < 10$ the response saturates, demonstrating that this is indeed a boundary effect. **b** Half-size maximum photo-induced phase difference, averaged over soliton and antisoliton initial conditions (represented in the inset), versus the inverse coordinate x_0^{-1} . Here the segment length is $L = 200$. Saturation to the soliton-free response (see the dashed horizontal line) is observed for $x_0^{-1} \lesssim 0.03$, whereas the response gradually decays for larger x_0^{-1} . The following (normalized) parameters are used in both plots: $V_0 = 3.5$, $q = 1.4 \times 10^{-4}$, $\alpha = 0.5$, and $\beta = 10^{-5}$.

virtue of the large value of the intrabilayer Josephson coupling. However, at higher temperatures, this is no longer a valid assumption. We can estimate the typical distance between two solitons through a high temperature expansion⁷⁷ to be given by in-plane coherence length, ξ .

For the single bilayer, we investigate the robustness of the light-induced paramagnetism phenomenon to (anti)solitons by repeating the SG calculations for $V_0 = 3.5$ and $q = 1.4 \times 10^{-4}$ using the initial conditions (in dimensionless form):

$$\theta(x, 0) = -q \frac{e^{-x} - e^{-(L-x)}}{1 + e^{-L}} + 4 \arctan e^{\pm(x-x_0)}, \quad (25)$$

where the first term encodes the static diamagnetic response within the segment, and the second term corresponds to a SG soliton (+) or antisoliton (−) at a distance x_0 from the $x = 0$ edge.

We work with $0 < x_0 < L/2$, and evaluate the system response in terms of the half-size maximum photo-induced phase difference, i.e., $\Delta\theta_{1/2,\text{ind}}^{\text{max}} = \max\{\theta|_{x=0}^{x=L/2} - \theta_{\text{eq}}|_{x=0}^{x=L/2}\}$. In particular, expecting the same average population of solitons and antisolitons, in Fig. 8(b) we plot $\Delta\theta_{1/2,\text{ind}}^{\text{max}}$ versus x_0^{-1} upon averaging over the two (\pm) different solitonic initial conditions, see also the sketch in the inset. Our mechanism shows robustness to the presence of (anti)solitons, as the response saturates to the soliton-free counterpart (see the dashed horizontal line) for $x_0^{-1} \sim 0.03$. Beyond this threshold, we observe a gradual suppression of the effect. In fact, when (anti)solitons are very close to the edge, they can interfere with the pre-soliton emergence, as well as scatter from the boundary, thereby leading to somewhat convoluted nonlinear

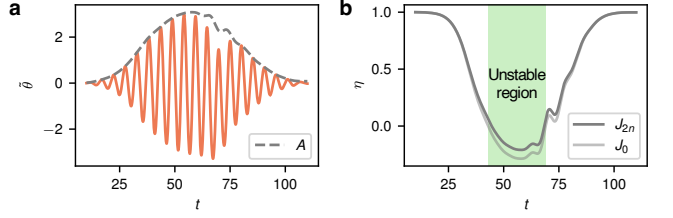


FIG. 9. **Homogeneous solution and parametric drive.** **a** $\tilde{\theta}$ trajectory (full line), and its smoothly varying envelope A (dashed line), versus time. **b** Parametric drive $\eta(A(t))$, comparing the J_0 -only result, see the light gray line, with that accounting for higher-frequency (J_{2n}) corrections, see the gray line. The green shaded area denotes the unstable, $\eta < 0$, region. The (normalized) parameters values $V_0 = 3.5$ and $\alpha = 0.5$ are used in both plots.

transients.

Floquet framework. According to Eqs. (6)–(8), the homogeneous solution $\tilde{\theta}$ follows the driven damped pendulum equation, and its slowly varying amplitude $A(t)$ enters the linearized dynamical equation for the inhomogeneous part θ' as a parametric drive $\eta(A)$. Specifically, as shown in Appendix 3, a Floquet expansion yields the expression:

$$\eta(A) = J_0(A) + 2 \sum_n \frac{J_{2n}(A)J_{-2n}(A) [(2n\omega_p)^2 - J_0(A)]}{[(2n\omega_p)^2 - J_0(A)^2 + \alpha^2(2n\omega_p)^2]}, \quad (26)$$

where J_i is the i -th Bessel function of the first kind.

We numerically solve for the $\tilde{\theta}$ trajectory, and subsequently extract a smoothly varying envelope $A(t)$ via a low-pass-filtered Hilbert transform, see Fig. 9(a). We are then in position to evaluate the parametric drive $\eta(A(t))$, which features a leading contribution, see the ‘ J_0 ’ term in Eq. (26), as well as higher-frequency corrections, see the ‘ J_{2n} ’ summation over n in Eq. (26). In this regard, in Fig. 9(b) we display the parametric drive relative to the time trace of Fig. 9(a), comparing the result coming from the leading contribution alone, see the light gray line, with that obtained by including the higher-frequency corrections for $n \leq 5$, see the gray line. The two plotted η curves qualitatively look similar: their equilibrium value is one, and they cross zero-reaching negative values—due to the strongly nonlinear drive, see the green shaded area in Fig. 9(b). The $\eta < 0$ region is responsible for the unstable behavior in the slow variable θ' , and therefore we expect the system’s response to be sensitive to the appreciable quantitative difference between the two results shown in Fig. 9(b).

We find that including higher-frequency corrections tames the instability by a noticeable amount (as compared to the J_0 -only result), bringing the Floquet theory into remarkably close agreement with the SG prediction, as discussed in the main text. As a side note, we observe that only the very first terms in the ‘ J_{2n} ’ summation are

seen to matter in the present scenario, which motivates our choice of evaluating the J_{2n} sum up to $n = 5$.

Numerical techniques. To computationally handle the PDEs (in general, systems of coupled PDEs) presented in this article, we formulate them as systems of coupled first-order ODEs by employing second-order finite-difference approximations for the space derivatives. For instance, considering the (single bilayer) SG case for the field $\theta(x, t)$, we discretize the spatial domain as N points separated by steps of length Δx , and we define the restriction $\theta(n\Delta x, t) \equiv \theta_n(t)$ for $n = 1, \dots, N$. We then obtain a set coupled first-order ODEs for the quantities $\partial_t \theta_n \equiv v_n(t)$ and $\partial_t v_n \equiv a_n(t)$, which can be solved via standard numerical routines, such as `scipy.integrate's` `odeint`, for a discrete set of M times separated by intervals of duration Δt .

For the single bilayer numerical runs, we typically use the following discretization steps values: $\Delta x \approx 0.05$ and $\Delta t \approx \Delta x/5$. We tested the reliability of our numerical findings in multiple ways: (i) we checked the stability and consistency of the simulation outcomes upon systematic variation of the Δx and Δt discretization steps; (ii) we performed extensive preliminary runs via two other independent numerical approaches, the first being an implicit implementation based on Thomas' algorithm and the other making use of `Mathematica's` `NDSolve`, and we observed close agreement between the different methods on the discussed phenomena; (iii) within the pre-soliton regime, we reproduced the relevant features of the output of the full nonlinear (SG) model by recasting the problem in the Floquet picture, as addressed above. Similar assessments were conducted also for the multi-bilayer runs, which are presented in this article only for the Floquet effective theory, using step sizes of $\Delta x \approx 0.1$ and $\Delta t \lesssim \sqrt{\beta} \Delta x/2$, the latter choice being determined by stability considerations on the linearized model.

As a concluding technical remark, we note that

throughout the paper, results are presented after convolution with a Gaussian profile over several driving periods. This reflects the fact that the experiments³² originally motivating our work use detectors that average over that timescale.

DATA AND CODE AVAILABILITY

The data presented in this work is produced directly by the codes provided below. The data can also be provided upon request.

An example of the code used to produce the data in the paper is openly available on GitHub, see Ref. 78.

ACKNOWLEDGEMENTS

We acknowledge fruitful discussion with Andrea Cavalleri, Michele Buzzi, Gergor Jotzu, Sebastian Fava, Giovanni De Vecchi, Walter Metzner, Andrew Millis, Subir Sachdev, Gil Refael, Pavel Dolgirev, Immanuel Bloch, Monika Aidelsburger, Leonid Rokhinson, Jukka Vayrynen, Yuli Lyanda-Geller, Hope Bretcher, Alex Potts, Claudio Guarcello, Davide Valenti, Bernardo Spagnolo, and Angelo Carollo. M.H.M. is grateful for the financial support received from the Alex von Humboldt postdoctoral fellowship. D.D.S. acknowledges the support of the Italian Ministry of University and Research (MUR) and ETH Zurich for the hospitality. E.A.D. acknowledges support from ETHZ, the SNSF project 200021_212899, the ARO grant number W911NF-21-1-0184, and NCCR SPIN (SNSF grant number 225153). P.A.L. acknowledges support from DOE (USA) office of Basic Sciences Grant No. DE-FG02-03ER46076.

COMPETING INTERESTS

The authors declare no competing interests.

APPENDIX 1: ELECTRODYNAMICS OF THE PSEUDOGAP BILAYER YBCO

Maxwell equations for the layered YBCO. As sketched in Fig. A.1, the YBCO structure consists of bilayers with spacing d_1 , which are separated from each other by a larger spacing d_2 . The unit cell dimension along the z -direction is $d_1 + d_2$. We shall employ the layer index $i = \{1, 2\}$ to denote the bottom and top members of a bilayer, and l to denote the l -th unit cell. We start our description by considering the Maxwell equations:

$$\frac{1}{c^2} \partial_t E_z + \frac{1}{c^2 \epsilon_0} j_z = \partial_x B_y, \quad (\text{A.1})$$

$$\frac{1}{c^2} \partial_t E_x + \frac{1}{c^2 \epsilon_0} j_x = \partial_z B_y, \quad (\text{A.2})$$

$$B_y = \partial_z A_x - \partial_x A_z, \quad (\text{A.3})$$

where we take the system to be homogeneous along the y -axis. To model the low-energy electrodynamics of the YBCO system, we assume that physical quantities are approximately constant between CuO layers and can be replaced by

their averages. For the z -component of the electric field, we thus focus on:

$$E_{z,1,l} = \frac{1}{d_1} \int_{z_{1,l}}^{z_{2,l}} dz E_z(z), \quad (\text{A.4})$$

$$E_{z,2,l} = \frac{1}{d_2} \int_{z_{2,l}}^{z_{1,l+1}} dz E_z(z). \quad (\text{A.5})$$

Similarly, for the y -component of the magnetic field we have that:

$$B_{y,1,l} = \frac{A_{x,2,l} - A_{x,1,l}}{d_1} - \partial_x A_{z,1,l}, \quad (\text{A.6})$$

$$B_{y,2,l} = \frac{A_{x,1,l} - A_{x,2,l}}{d_2} - \partial_x A_{z,2,l}, \quad (\text{A.7})$$

where we have defined $A_{x,1,l} = A_x(z = z_{1,l})$, $A_{x,2,l} = A_x(z = z_{2,l})$, $A_{z,1,l} = \frac{1}{d_1} \int_{z_{1,l}}^{z_{2,l}} dz A_z(z)$, and $A_{z,2,l} = \frac{1}{d_2} \int_{z_{2,l}}^{z_{1,l+1}} dz A_z(z)$. Moreover, we assume that the current along the x -direction is localised at each CuO layer:

$$j_x(z) = \sum_l [j_{x,1,l} \delta(z - z_{1,l}) + j_{x,2,l} \delta(z - z_{2,l})]. \quad (\text{A.8})$$

Integrating Eq. (A.1) over d_1 (distance between layers) and Eq. (A.2) across the layer thickness, we find a set of closed equations in terms of the intra-bilayer and inter-bilayer fields:

$$\frac{1}{c^2} \partial_t E_{z,1,l} + \frac{1}{c^2 \epsilon_0} j_{z,1,l} = \partial_x B_{y,1,l}, \quad (\text{A.9})$$

$$\frac{1}{c^2} \partial_t E_{z,2,l} + \frac{1}{c^2 \epsilon_0} j_{z,2,l} = \partial_x B_{y,2,l}, \quad (\text{A.10})$$

$$\frac{1}{c^2 \epsilon_0} j_{x,1,l} = B_{y,2,l-1} - B_{y,1,l}, \quad (\text{A.11})$$

$$\frac{1}{c^2 \epsilon_0} j_{x,2,l} = B_{y,1,l} - B_{y,2,l}, \quad (\text{A.12})$$

where the average currents along the z -direction are given by $j_{z,1,l} = \frac{1}{d_1} \int_{z_{1,l}}^{z_{2,l}} j_z(z)$ and $j_{z,2,l} = \frac{1}{d_2} \int_{z_{2,l}}^{z_{1,l+1}} j_z(z)$.

Dissipationless counter-flow model for pseudogap YBCO. The dissipationless counter-flow is modelled by a superfluid response in plane, with a friction force created by the motion of pancake vortices⁶⁹. According to Ref. 48, vortices flow only due to the sum of the currents in the two bilayers. When the currents are anti-symmetric, intra-bilayer coherence can pin the vortices in the two layers, allowing the counter-flow current to remain dissipationless. This scenario is captured by the superfluid equations:

$$\partial_t j_{z,1,l}^s = \frac{e^*}{\hbar} d_1 J_{c,1} \cos(\theta_{1,l}) E_{z,1,l}, \quad (\text{A.13})$$

$$\partial_t j_{z,2,l}^s = \frac{e^*}{\hbar} d_2 J_{c,2} \cos(\theta_{2,l}) E_{z,2,l}, \quad (\text{A.14})$$

$$\partial_t j_{x,1,l}^s = \frac{(e^*)^2 n_s}{m} E_{x,1,l} + \gamma_d (j_{x,1,l}^s + j_{x,2,l}^s), \quad (\text{A.15})$$

$$\partial_t j_{x,2,l}^s = \frac{(e^*)^2 n_s}{m} E_{x,2,l} + \gamma_d (j_{x,1,l}^s + j_{x,2,l}^s), \quad (\text{A.16})$$

where $\theta_{1,l} = \phi_{2,l} - \phi_{1,l} - \frac{e^*}{\hbar} d_1 A_{z,1,l}$ and $\theta_{2,l} = \phi_{1,l+1} - \phi_{2,l} - \frac{e^*}{\hbar} d_2 A_{z,2,l}$ are the gauge invariant phases, directly related to the electric fields through the relations $\hbar \partial_t \theta_{1,l} = e^* d_1 E_{z,1,l}$ and $\hbar \partial_t \theta_{2,l} = e^* d_2 E_{z,2,l}$, $E_{x,1,l} = E_x(z = z_{1,l})$ and $E_{x,2,l} = E_x(z = z_{2,l})$ are the in-plane electric fields, n_s is the 2D superfluid density in each CuO-layer, and γ_d is a friction coefficient accounting for the vortex motion in the presence of a symmetric current in each bilayer. In the counter-flow state, we take $J_{c,2} = 0$ and assume that the bilayer Josephson coupling is unaffected, i.e., $J_{c,1} = J_{c,1}(T = 0 \text{ K})$.

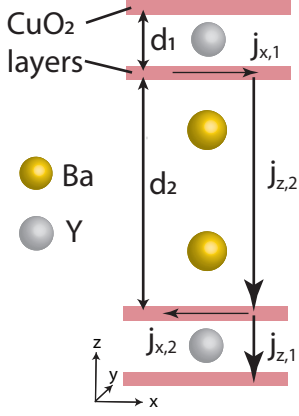


FIG. A.1. **Sketch of YBCO.** The crystal structure of YBCO is made up of pairs of CuO_2 -layers that below T_c become superconducting. Members of a CuO_2 bilayer are separated by an Yttrium atom and an inter-layer distance of $d_1 = 4 \text{ \AA}$, while different bilayers are separated by two Barium atoms and a distance of $d_2 = 4 \text{ \AA}$. In the figure we also annotated the position of the in-plane and out-of-plane currents.

We henceforth examine the system's response at momentum $q_z = 0$, where the fields have the same amplitude in each unit cell, and drop the l -index dependence. Equations (A.11) and (A.12) always imply equal and opposite in-plane currents, $j_{x,2} = -j_{x,1}$, thereby leading to dissipationless in-plane relative phase dynamics. Dissipation is nevertheless included as $j_{z,1}^n = \sigma_{n,1}E_{z,1}$ and $j_{z,2}^n = \sigma_{n,2}E_{z,2}$, where $\sigma_{n,1}$ is the normal c-axis bilayer conductivity and $\sigma_{n,2}$ is a similar quantity motivated by the cavity to the radiation field formed by the region in-between bilayers being leaky. The cavity Q leads to dissipation of photon modes, which can be modeled by adding a term proportional to the intra-bilayer electric field in Eq. (A.10). This will lead to a dissipative term parametrized by $\sigma_{n,2}$ in the equation for θ_2 below. Note that $\sigma_{n,2}$ is a parameter that models the cavity Q and should not be interpreted as conductivity between bilayers.

Equations (A.11)–(A.12) express the discontinuity of the magnetic field B_y across each layer in terms of the in-plane current. The latter can be formulated through θ and B_y by writing the electric field along the x -direction in terms of the gauge invariant phase, $\partial_t(\hbar\partial_x\phi_1 - e^*A_{x,1}) = e^*E_{x,1}$ and $\partial_t(\hbar\partial_x\phi_2 - e^*A_{x,2}) = e^*E_{x,2}$, and using Eqs. (A.15)–(A.16) and Eqs. (A.6)–(A.7). Equations (A.11)–(A.12) become

$$\beta \left(\partial_x\theta_1 - \frac{e^*}{\hbar}d_1B_{y,1} \right) = B_{y,1} - B_{y,2}, \quad (\text{A.17})$$

$$\frac{d_2}{d_1}\beta \left(\partial_x\theta_2 - \frac{e^*}{\hbar}d_2B_{y,2} \right) = B_{y,2} - B_{y,1} \quad (\text{A.18})$$

where $\beta = \frac{(e^*)^2n_sd_1}{2\epsilon_0mc^2}$. We use Eqs. (A.17) and (A.18) to solve for $B_{y,1}$ and $B_{y,2}$ in terms of θ_1 and θ_2 . Plugging into Eqs. (A.9) and (A.10), we arrive at the equations of motion for the gauge invariant phases in the pseudogap counter-flow state:

$$\frac{1}{c^2}\partial_t^2\theta_1 + \frac{\omega_{J,1}^2}{c^2}\sin\theta_1 + \frac{\sigma_{n,1}}{\epsilon_0c^2}\partial_t\theta_1 - \frac{1}{d_2(1+\beta)+d_1}\partial_x^2[(d_1+d_2\beta)\theta_1 + d_1\theta_2] = 0, \quad (\text{A.19})$$

$$\frac{1}{c^2}\partial_t^2\theta_2 + \frac{\sigma_{n,2}}{\epsilon_0c^2}\partial_t\theta_2 - \frac{1}{d_2(1+\beta)+d_1}\partial_x^2[d_2(1+\beta)\theta_2 + d_2\theta_1] = 0, \quad (\text{A.20})$$

which depend on the frequency of the upper plasmon $\omega_{J,1} \approx 2\pi \times 14 \text{ THz}$, the intra-bilayer distance $d_1 \approx 4 \text{ \AA}$, the inter-bilayer distance $d_2 \approx 8 \text{ \AA}$, and the dimensionless parameter β . In Appendix 2, we show that the value $\beta \approx 10^{-5}$ can be estimated from experiments as the diamagnetic response of the pseudogap phase due to counter-flow screening.

External driving. In the presence of an homogeneous pump electric field along the z -direction, $E_p = E_0f(t)$, the currents along the z -direction are given by:

$$j_{z,1}^s = J_{c,1}\sin\left(\theta_1 - \frac{e^*}{\hbar}d_1A_{p,1}\right), \quad (\text{A.21})$$

$$j_{z,i}^n = \frac{\sigma_{n,i}}{e^*d_i}\partial_t\left(\theta_i - \frac{e^*}{\hbar}d_iA_{p,i}\right), \quad (\text{A.22})$$

where $i = \{1, 2\}$, $\partial_t A_{p,1} = -E_p$, and $\partial_t A_{p,2} = -E_p$. This leads to the driven equations of motion:

$$\frac{1}{c^2}\partial_t^2\theta_1 + \frac{\omega_{J,1}^2}{c^2}\sin\left(\theta_1 - \frac{e^*}{\hbar}d_1A_{p,1}\right) + \frac{\sigma_{n,1}}{\epsilon_0c^2}\partial_t\left(\theta_1 - \frac{e^*}{\hbar}d_1A_{p,1}\right) - \frac{1}{d_2(1+\beta)+d_1}\partial_x^2[(d_1+d_2\beta)\theta_1 + d_1\theta_2] = 0, \quad (\text{A.23})$$

$$\frac{1}{c^2}\partial_t^2\theta_2 + \frac{\sigma_{n,2}}{\epsilon_0c^2}\partial_t\left(\theta_2 - \frac{e^*}{\hbar}d_2A_{p,2}\right) - \frac{1}{d_2(1+\beta)+d_1}\partial_x^2[d_2(1+\beta)\theta_2 + d_2\theta_1] = 0. \quad (\text{A.24})$$

The latter equations can be expressed in a simpler form via the uniform transformation $\theta_1 = \Theta_1 + \frac{e^*}{\hbar} d_1 A_{p,1}$ and $\theta_2 = \Theta_2 + \frac{e^*}{\hbar} d_2 A_{p,2}$:

$$\frac{1}{c^2} \partial_t^2 \Theta_1 + \frac{\omega_{J,1}^2}{c^2} \sin \Theta_1 + \frac{\sigma_{n,1}}{\epsilon_0 c^2} \partial_t \Theta_1 - \frac{1}{d_2(1+\beta) + d_1} \partial_x^2 [(d_1 + d_2\beta)\Theta_1 + d_1\Theta_2] = \frac{e^* d_1}{\hbar c^2} \partial_t E_p(t), \quad (\text{A.25})$$

$$\frac{1}{c^2} \partial_t^2 \Theta_2 + \frac{\sigma_{n,2}}{\epsilon_0 c^2} \partial_t \Theta_2 - \frac{1}{d_2(1+\beta) + d_1} \partial_x^2 [d_2(1+\beta)\Theta_2 + d_2\Theta_1] = \frac{e^* d_2}{\hbar c^2} \partial_t E_p(t). \quad (\text{A.26})$$

In this basis, the equations of motion resemble that solved for coupled systems of driven damped long Josephson junctions^{34–36,38,39}.

Boundary conditions for a periodic bilayer system of finite width. To account for the physics between two cracks, it is necessary to define the boundary conditions that simulate the electrodynamics outside the pumped finite segment. Indeed, as local paramagnetic currents are formed and amplified within the pre-soliton regime, an equal and opposite flux is anticipated to stem from the boundaries, ensuring conservation of the total flux. The boundary conditions at the $x = 0$ interface are expressed as follows²¹:

$$E_{z,\text{air},q_z=0}|_{x=0} = E_{z,\text{mat},q_z=0}|_{x=0}, \quad (\text{A.27})$$

$$B_{y,\text{air},q_z=0}|_{x=0} = B_{y,\text{mat},q_z=0}|_{x=0}, \quad (\text{A.28})$$

$$j_{x,1}|_{x=0} \propto (B_{y,2} - B_{y,1})|_{x=0} = 0, \quad (\text{A.29})$$

where the first two conditions state that the tangential components of the average electric and magnetic fields are continuous across the interface. We break up the fields in air as externally imposed contributions plus propagating modes:

$$E_{z,\text{air},q_z=0}|_{x=0} = E_{\text{air},q_x}|_{x=0} + E_p, \quad (\text{A.30})$$

$$B_{y,\text{air},q_z=0}|_{x=0} = B_{\text{air},q_x}|_{x=0} + B_{\text{ext}}. \quad (\text{A.31})$$

For a left (right) propagating mode, we have the condition $B_{\text{air},q_x} = +(-) \frac{1}{c} E_{\text{air},q_x}$, implying:

$$B_{y,\text{mat},q_z=0}|_{x=0} - B_{\text{ext}} = +(-) \frac{1}{c} [E_{z,\text{mat},q_z=0}|_{x=0} - E_p]. \quad (\text{A.32})$$

Taking the average electric field as $E_{z,\text{mat},q_z=0} = \hbar \frac{\partial_t \Theta_1 + \partial_t \Theta_2}{e^*(d_1 + d_2)} = \hbar \frac{\partial_t \theta_1 + \partial_t \theta_2}{e^*(d_1 + d_2)} + E_p$, we get the following boundary conditions:

$$\left\{ \partial_x \Theta_1 + \partial_x \Theta_2 \mp \frac{1}{c} [\partial_t \Theta_1 + \partial_t \Theta_2 - e^*(d_1 + d_2) E_p] \right\} \Big|_{x=0,L} = \frac{e^*(d_1 + d_2)}{\hbar} B_{\text{ext}}, \quad (\text{A.33})$$

$$\left(\frac{\partial_x \Theta_1}{d_1} - \frac{\partial_x \Theta_2}{d_2} \right) \Big|_{x=0,L} = 0, \quad (\text{A.34})$$

where the $-$ ($+$) sign applies to the $x = 0$ ($x = L$) boundary. Throughout this work, we report Eqs. (A.25)–(A.26) and Eqs. (A.33)–(A.34) and drop the capitals, i.e., we redefine $\Theta_1 \equiv \theta_1$ and $\Theta_2 \equiv \theta_2$.

Single bilayer limit. Above, we have derived the electromagnetic equations of motion for a multi-bilayer system. A physically instructive limit to take is that of a single bilayer. To this end, we let $d_2 \rightarrow \infty$, obtaining the intra-bilayer equation:

$$\frac{1}{c^2} \partial_t^2 \theta + \frac{\omega_J^2}{c^2} \sin \theta + \frac{\sigma_n}{\epsilon_0 c^2} \partial_t \theta - \frac{\beta}{1+\beta} \partial_x^2 \theta = \frac{e^* d_1}{\hbar c^2} \partial_t E_p, \quad (\text{A.35})$$

where (as in the main text) we suppressed the ‘1’ subscript: $\theta_1 \equiv \theta$, $\omega_{J,1} \equiv \omega_J$, and $\sigma_{n,1} \equiv \sigma_n$. As the previous equation indicates, in this limit, the bilayer dynamics is decoupled from that in-between the bilayers. The resulting equation, referred to in the literature as the perturbed (or driven damped) SG equation^{36,38,39}, captures the instabilities discussed in the main text. The multi-bilayer solution then yields corrections to the SG prediction, accounting for the capacitive coupling between layers. The inter-bilayer dynamics is described by:

$$\partial_t^2 \theta_2 + \frac{\sigma_{n,2}}{\epsilon_0} \partial_t \theta_2 - c^2 \partial_x^2 \theta_2 = \frac{c^2}{1+\beta} \partial_x^2 \theta + \frac{e^* d_2}{\hbar} \partial_t E_p. \quad (\text{A.36})$$

This highlights that capacitive coupling between neighboring layers remains significant in the present limit and reinforces the observation that, for large but finite d_2 , the current generated within the bilayer is converted into a displacement current between bilayers, resulting in the overall edge current discussed in the main text.

APPENDIX 2: EQUILIBRIUM COUNTER-FLOW DIAMAGNETISM

Here we consider a semi-infinite geometry with a interface to air at $x = 0$. In the presence of a magnetic field, the boundary conditions are given by $B_{y,1}|_{x=0} = B_{y,2}|_{x=0} = B_{\text{ext}}$. In terms of the gauge invariant phases, we get:

$$\partial_x \theta_1|_{x=0} = \frac{e^* d_1}{\hbar} B_{\text{ext}}, \quad (\text{A.37})$$

$$\partial_x \theta_2|_{x=0} = \frac{e^* d_2}{\hbar} B_{\text{ext}}. \quad (\text{A.38})$$

To analytically solve the equilibrium problem, it is simpler work directly with the magnetic fields, which using Eqs. (A.17) and (A.18) are found to satisfy:

$$\partial_x^2 B_{y,1} = \left(\frac{\omega_{J,1}^2}{c^2} \cos \theta_1 + \frac{1}{c^2} \partial_t^2 + \frac{\sigma_{n,1}}{\epsilon_0 c^2} \partial_t \right) \left(\frac{B_{y,1} - B_{y,2}}{\beta} + B_{y,1} \right), \quad (\text{A.39})$$

$$\partial_x^2 B_{y,2} = \left(\frac{1}{c^2} \partial_t^2 + \frac{\sigma_{n,2}}{c^2} \partial_t \right) \left(\frac{B_{y,2} - B_{y,1}}{\beta \frac{d_2}{d_1}} + B_{y,2} \right). \quad (\text{A.40})$$

In the static limit θ_1 is small, such that $\cos \theta_1 \approx 1$, and our equations become:

$$\partial_x^2 B_{y,1} = \frac{\omega_{J,1}^2}{c^2} \left(\frac{B_{y,1} - B_{y,2}}{\beta} + B_{y,1} \right), \quad (\text{A.41})$$

$$\partial_x^2 B_{y,2} = 0. \quad (\text{A.42})$$

Solutions of the latest system of equations are readily obtained as:

$$B_{y,1}(x) = (B_{\text{ext}} - B_{\text{sc}}) e^{-kx} + B_{\text{sc}}, \quad (\text{A.43})$$

$$B_{y,2}(x) = B_{\text{ext}}, \quad (\text{A.44})$$

where $B_{\text{sc}} = \frac{1}{1+\beta} B_{\text{ext}}$ is the screened field and $k = \lambda^{-1} = \frac{\omega_{J,1}}{c} \sqrt{\frac{1+\beta}{\beta}}$ is the inverse penetration depth. These solutions imply that, inside the bilayer, we have a diamagnetic susceptibility given by $\chi_{\text{bilayer}} = -\beta$. Since the bilayer makes up 1/3 of the unit cell, the effective diamagnetic susceptibility of the entire structure due to counter-flow currents is given by:

$$\chi_d = -\frac{\beta}{3}. \quad (\text{A.45})$$

According to Ref. 43, which reports on measurements of magnetic properties of YBCO, there exists an excess diamagnetic contribution of $\chi_d = -10^{-5}$ in the pseudogap regime. Assuming that such value originates entirely from the counter-flow diamagnetism described here, we arrive to $\beta = 3 \times 10^{-5}$.

In the single bilayer limit, $d_2 \rightarrow \infty$, the following expression holds for the magnetic field $B_{y,1}$:

$$B_{y,2} - B_{y,1}(x) = \frac{\beta}{1+\beta} \left(B_{\text{ext}} - \frac{\hbar}{e^* d_1} \partial_x \theta_1 \right) \quad (\text{A.46})$$

and the in-plane screening currents are:

$$\frac{1}{c^2 \epsilon_0} j_{x,1} = -\frac{1}{c^2 \epsilon_0} j_{x,2} = B_{y,2} - B_{y,1} = \frac{\beta}{1+\beta} \left(B_{\text{ext}} - \frac{\hbar}{e^* d_1} \partial_x \theta_1 \right). \quad (\text{A.47})$$

APPENDIX 3: FLOQUET EFFECTIVE THEORY FOR THE SG PRE-SOLITON REGIME

We decompose the solutions of the perturbed SG model as $\theta(x, t) = \tilde{\theta}(t) + \theta'(x, t)$, where $\tilde{\theta}$ is a spatially homogeneous oscillating component obeying the driven damped pendulum equation (in rescaled units, $x \rightarrow x/\lambda$ and $t \rightarrow t \omega_J$, see the main text):

$$\partial_t^2 \tilde{\theta} + \alpha \partial_t \tilde{\theta} + \sin \tilde{\theta} = \partial_t V(t), \quad (\text{A.48})$$

while θ' satisfies the inhomogeneous boundary conditions and is subject to the effective SG potential created by the oscillations of $\tilde{\theta}$:

$$\partial_t^2 \theta' + \alpha \partial_t \theta' + \cos \tilde{\theta} \sin \theta' + (\cos \theta' - 1) \sin \tilde{\theta} = 0, \quad (\text{A.49})$$

$$\partial_x \theta'|_{x=0,L} = q. \quad (\text{A.50})$$

We then approximate $\tilde{\theta}(t)$ as a function oscillating with frequency ω_p , but with a slowly time-varying amplitude (that is, on the timescale of the pump's envelope):

$$\tilde{\theta}(t) = A(t) \sin(\omega_p t). \quad (\text{A.51})$$

For a fixed amplitude A , we can expand the nonlinear SG potential into harmonics oscillating at multiples of ω_p :

$$\cos[A \sin(\omega_p t)] = J_0(A) + \sum_n J_{2n}(A) e^{-i2n\omega_p t}. \quad (\text{A.52})$$

Even if the pump's amplitude is very large, in the range of small q of interest for experimental purposes (see the main text), the dynamical equation for θ' can be linearized. The resulting effective equation of motion, in frequency space, takes the form:

$$[-\omega^2 + i\alpha\omega + J_0(A)] \theta'(\omega) + \sum_n [J_{2n}(A) \theta'(\omega + 2n\omega_p) + J_{-2n} \theta'(\omega - 2n\omega_p)] = 0, \quad (\text{A.53})$$

where different frequency components of θ' are coupled to all the Floquet copies. Restricting ω to the first Brillouin zone of the Floquet problem, $\omega \in (-\omega_p/2, \omega_p/2)$, we can express different Floquet components using the notation, $\theta'^{(n)} = \theta'(\omega + n\omega_p)$. By means of a Floquet perturbation theory⁷⁹, we can include the effects of higher θ' harmonics on the dynamics of the slowly varying $\theta'^{(0)}(\omega)$, up to second order in the off-diagonal components $J_{2n}(A)$. Assuming $\omega \ll \omega_p$, the equations of motion become, to leading order:

$$[-\omega^2 + i\alpha\omega + J_0(A)] \theta'^{(0)} + J_{2n}(A) \theta'^{(2n)} + J_{-2n}(A) \theta'^{(-2n)} = 0, \quad (\text{A.54})$$

$$[-(2n\omega_p)^2 + i\alpha 2n\omega_p + J_0(A)] \theta'^{(2n)} = -J_{-2n}(A) \theta'^{(0)}, \quad (\text{A.55})$$

Combining the two equations together, we find the effective equation for $\theta'^{(0)}$, to second order in the Floquet expansion:

$$[-\omega^2 + i\alpha\omega + J_0(A)] \theta'^{(0)} - J_{2n}(A) J_{-2n}(A) \left[\frac{1}{-(2n\omega_p)^2 + i\alpha 2n\omega_p + J_0(A)} + \frac{1}{-(2n\omega_p)^2 - i\alpha 2n\omega_p + J_0(A)} \right] \theta'^{(0)} = 0, \quad (\text{A.56})$$

$$[-\omega^2 + i\alpha\omega + J_0(A)] \theta'^{(0)} + 2J_{2n}(A) J_{-2n}(A) \left\{ \frac{(2n\omega_p)^2 - J_0(A)}{[(2n\omega_p)^2 - J_0(A)]^2 + \alpha^2 (2n\omega_p)^2} \right\} \theta'^{(0)} = 0. \quad (\text{A.57})$$

This leads to a parametric drive term η :

$$\eta(A) = J_0(A) + 2 \sum_n J_{2n}(A) J_{-2n}(A) \left\{ \frac{(2n\omega_p)^2 - J_0(A)}{[(2n\omega_p)^2 - J_0(A)]^2 + \alpha^2 (2n\omega_p)^2} \right\}. \quad (\text{A.58})$$

In practice, we solve for $\tilde{\theta}$ numerically, and then extract its envelope via a Hilbert transform. Due to the nonlinear nature of the pendulum equation, $\tilde{\theta}$ is not described just by a single harmonic, $\tilde{\theta} = A \sin(\omega_p t)$, but in general higher harmonic contributions will come into play. Indeed, the envelope we compute usually presents some fast components on top of a smooth background. We neglect such higher harmonic contributions by employing a low-pass filter. We find this scheme to provide a simple yet accurate approximation for most of our purposes; however, at very large pump amplitudes, the neglected higher harmonics should also be included in the Floquet analysis.

APPENDIX 4: DYNAMICAL SG RESPONSE

Dynamically excited SG solitons and pre-solitons. In Fig. A.2(a) and (b), we present contour plots of the phase and its gradient, respectively, to illustrate how solitons can enter the system through the cooperative action of a small

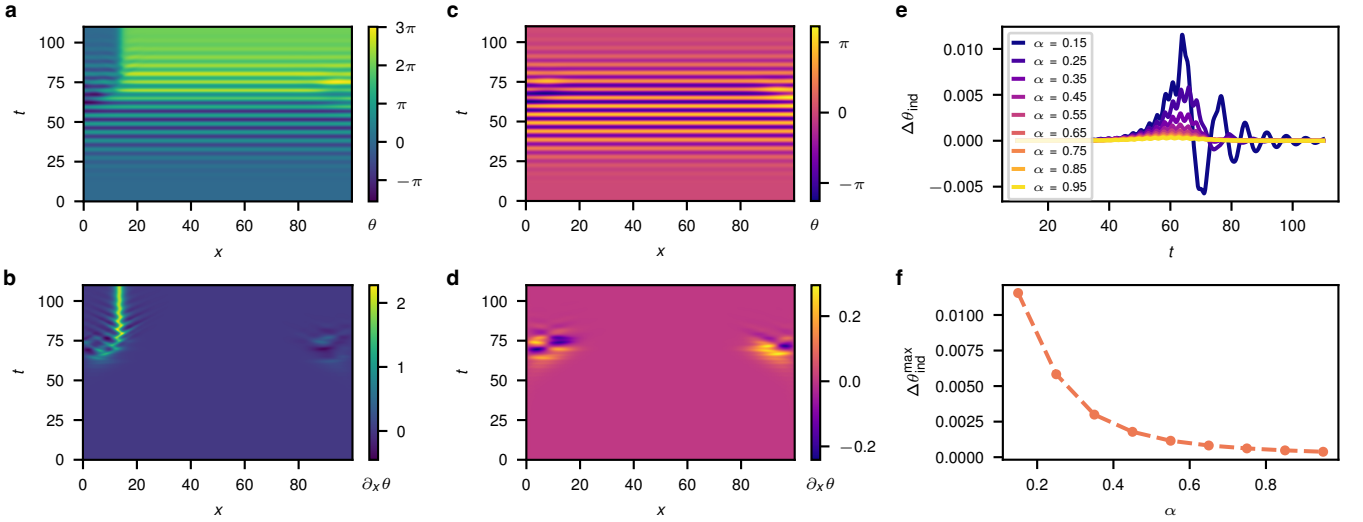


FIG. A.2. Spatio-temporal behaviors and damping dependence in the driven SG model. **a** Contour plot of the phase and **b** contour plot of the phase gradient for the (normalized) parameter combination $V_0 = 4$ and $q = 0.01$, representative of the soliton regime, discussed in the main text. Under driving, small boundary inhomogeneities caused by nonzero-flux boundary conditions gradually increase until a soliton, located around $x = 10$ in this example, is excited. **c** Contour plot of the phase and **d** contour plot of the phase gradient for the combination $V_0 = 3.5$ and $q = 0.01$, taken in the pre-soliton scenario. An edge-localized excitation, qualitatively similar to a soliton but with much smaller amplitude, develops during pumping. The following (dimensionless) parameters are used in panels (a)-(d): $L = 100$, $\alpha = 0.5$, and $\beta = 10^{-5}$. **e** Time traces of the photo-induced phase difference across the entire segment and **f** maximum photo-induced phase difference versus the damping coefficient, for $V_0 = 2.5$, $q = 1.4 \times 10^{-4}$, $L = 100$, and $\beta = 10^{-5}$. As dissipation decreases, we observe an enhancement in the system's peak pre-solitonic response. The lower dissipation scenario, however, is also characterized by more pronounced oscillatory transients.

boundary field and strong spatially uniform driving. The latter induces an fast oscillating background, over which initial boundary-localized profiles surf and get amplified. This eventually leads to the penetration of a full soliton, located at $x \approx 10$ in the shown example, as indicated by the 2π phase step or equivalently by the peak gradient response of roughly 2. We note in passing that the soliton, if formed sufficiently away from the edge, persists long after the pump pulse has passed by virtue of its topological robustness. In Fig. A.2(c) and (d), we show the spatio-temporal phase and gradient profiles for a case representative of the pre-soliton regime. Here, in the presence of strong driving, a soliton-like structure emerges out of the equilibrium configuration, which is characterized by very small gradients at the edges and is zero elsewhere, surfing over the (pump-induced) uniform oscillations. In this scenario, the localized feature we refer to as pre-soliton has a much smaller amplitude than an actual SG soliton, and it fades away once the pump pulse is gone at a rate influenced by the damping coefficient.

Damping dependence within the SG pre-soliton regime. We now address the sensitivity of our SG pre-soliton results to damping, by varying the α parameter over an order of magnitude: $\alpha \in (0.1, 1)$. As shown in Fig. A.2(e), the time traces of the photo-induced phase difference indicate a more pronounced overall response as dissipation is decreased, with both larger peak values and oscillations on the way back to equilibrium. It should be pointed out that, to precisely illustrate the dynamical traits under discussion, here we do not perform any convolution operation on the simulation results, as opposed to what is mostly done elsewhere in this work (e.g., in the main text's plots, oscillations at a period of $\sim 1/\omega_p$ during the pre-solitonic build-up are filtered out). The results' dependence on α is further highlighted by considering the peak response, see Fig. A.2(f). In this case, we observe a power-law-type attenuation of the maximum photo-induced phase difference with the dissipation strength. In general, as previously hinted in our work, the $\alpha \rightarrow 0$ limit can be rather subtle: as exploring the full SG excitation spectrum progressively becomes easier, complications to the simple instability picture painted above can gradually arise. For example, the emergence of long-lived (for $\alpha \rightarrow 0$) breather-like modes can enhance the oscillatory character of the $\Delta\theta_{\text{ind}}$ time traces, as compared to the mostly positive result obtained in the medium-to-large dissipation range.

APPENDIX 5: FLOQUET MULTI-BILAYER RESPONSE

Multi-bilayer Floquet effective framework. We start from Eqs. (A.25) and (A.26) derived above, which we now write in rescaled units, $x \rightarrow x/\lambda$ and $t \rightarrow t\omega_{J,1}$:

$$\partial_t^2\theta_1 + \sin\theta_1 + \alpha_1\partial_t\theta_1 - \frac{1+\beta}{\beta}\partial_x^2(K_1^+\theta_1 + K_2\theta_2) = \partial_t V(t), \quad (\text{A.59})$$

$$\partial_t^2\theta_2 + \alpha_2\partial_t\theta_2 - \frac{1+\beta}{\beta}\partial_x^2(K_2^+\theta_2 + K_1\theta_1) = \frac{d_2}{d_1}\partial_t V(t), \quad (\text{A.60})$$

where $K_1^+ = \frac{d_1+d_2\beta}{d_2(1+\beta)+d_1}$, $K_2 = \frac{d_1}{d_2(1+\beta)+d_1}$, $K_2^+ = \frac{d_2(1+\beta)}{d_2(1+\beta)+d_1}$, and $K_1 = \frac{d_2}{d_2(1+\beta)+d_1}$. We decompose our phase profiles as $\theta_{1,2}(x, t) = \tilde{\theta}_{1,2}(t) + \theta'_{1,2}(x, t)$, with the spatially homogeneous components defined as the solutions of the following equations:

$$\partial_t^2\tilde{\theta}_1 + \sin\tilde{\theta}_1 + \alpha_1\partial_t\tilde{\theta}_1 = \partial_t V(t), \quad (\text{A.61})$$

$$\partial_t^2\tilde{\theta}_2 + \alpha_2\partial_t\tilde{\theta}_2 = \frac{d_2}{d_1}\partial_t V(t), \quad (\text{A.62})$$

and the boundary-condition-sensitive components obeying:

$$\partial_t^2\theta'_1 + \eta\theta'_1 + \alpha_1\partial_t\theta'_1 - \frac{1+\beta}{\beta}\partial_x^2(K_1^+\theta'_1 + K_2\theta'_2) = 0, \quad (\text{A.63})$$

$$\partial_t^2\theta'_2 + \alpha_2\partial_t\theta'_2 - \frac{1+\beta}{\beta}\partial_x^2(K_2^+\theta'_2 + K_1\theta'_1) = 0, \quad (\text{A.64})$$

where the equation of motion of θ'_1 is linearized via the Floquet approach illustrated above, such that η is a parametric drive term that we extract from the driven damped pendulum solution. We evaluate the ratio between the z -averaged magnetic field within the unit cell and the equilibrium diamagnetic field amplitude as:

$$\frac{B_y}{|B_{\text{ext}}\chi_d|} = \frac{d_1 B_{y,1} + d_2 B_{y,2}}{(d_1 + d_2) |B_{\text{ext}}\chi_d|} = \frac{d_1}{d_1 + d_2} \frac{\partial_x\theta'_1 + \partial_x\theta'_2}{|q\chi_d|}. \quad (\text{A.65})$$

We can conveniently apply a shift to the inter-bilayer phase gradient, $\partial_x\theta'_2 \rightarrow \partial_x\theta'_2 - q\left(\frac{d_2}{d_1} + \frac{1}{1+\beta}\right)$, which does not influence the dynamical equations, so that we get:

$$\frac{d_1}{d_1 + d_2} \frac{\partial_x\theta'_1 + \partial_x\theta'_2}{|q\chi_d|} = \frac{d_1 (B_{y,1} - B_{\text{sc}}) + d_2 (B_{y,2} - B_{\text{ext}})}{(d_1 + d_2) |B_{\text{ext}}\chi_d|} \sim \frac{B_{\text{ind}}}{|B_{\text{ext}}\chi_d|}. \quad (\text{A.66})$$

In other words, our gradient shift amounts to subtracting off the bulk equilibrium contribution when computing the average magnetic field. We conclude this brief survey by listing the boundary conditions we use in our Floquet calculations:

$$\partial_x\theta'_1|_{x=0,L} = q \pm \sqrt{\frac{\beta}{1+\beta}} \frac{d_1}{d_1 + d_2} (\partial_t\theta'_1 + \partial_t\theta'_2)|_{x=0,L}, \quad (\text{A.67})$$

$$\partial_x\theta'_2|_{x=0,L} = -\frac{q}{1+\beta} \pm \sqrt{\frac{\beta}{1+\beta}} \frac{d_2}{d_1 + d_2} (\partial_t\theta'_1 + \partial_t\theta'_2)|_{x=0,L}, \quad (\text{A.68})$$

where the $+$ ($-$) sign applies to the $x = 0$ ($x = L$) edge and we neglect the fast E_p oscillations in Eq. (A.33). We note that, by taking $c \rightarrow c/n$ in Eq. (A.33), we can model propagation in an exterior medium with refractive index n , and the limit $n \rightarrow 0$ approaches Neumann boundary conditions. Throughout this work we use the value $n = 1$ unless stated otherwise.

Representative case. In Fig. A.3(a), (b), and (c), we report contour plots illustrating the typical spatio-temporal behavior of, respectively, the intra-bilayer phase θ'_1 , the inter-bilayer phase θ'_2 , and the magnetic field ratio $B_{\text{ind}}/|B_{\text{ext}}\chi_d|$, see Eq. (A.66). The phases θ'_1 and θ'_2 are enhanced in opposite directions during the pump, with θ'_1 growing negatively and θ'_2 positively at the $x = 0$ boundary, which is the focus of Fig. A.3(a) and (b) (similar features, with opposite signs w.r.t. that at $x = 0$, dynamically emerge also at $x = L$). While their profiles are mostly concentrated within

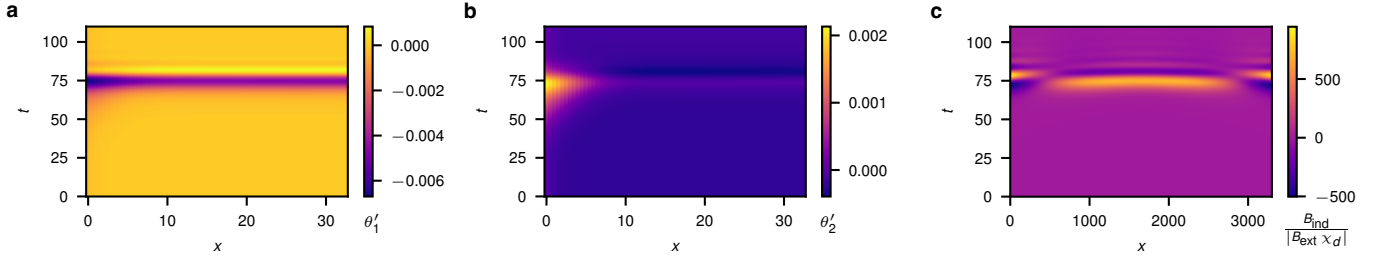


FIG. A.3. **Multi-bilayer spatio-temporal behaviors.** **a** Contour plot of the intra-bilayer phase θ'_1 , **b** contour plot of the inter-bilayer phase θ'_2 , and **c** contour plot of the average magnetic field induced within a unit cell, B_{ind} , normalized by the equilibrium diamagnetic field amplitude, $|B_{\text{ext}}\chi_d|$. Upon pumping, θ'_1 and θ'_2 monotonically grow in opposite directions (with θ'_1 increasing negatively and θ'_2 positively at the left edge), their profiles are mainly localized within a few penetration depths, but θ'_1 develops an appreciable tail into the bulk of the segment. The magnetic field originates from edge currents, as explicitly addressed in the main text, and it propagates from the system's boundaries inwards at the speed of light. Oscillations at the edges of the segment represent the field emitted by the strip. These three plots are obtained for the parameter set (identical to that of Fig. 4 in the main text): $L = 3300$, $V_0 = 3.5$, $q = 2.3 \times 10^{-4}$, $\alpha_1 = 0.4$, $\alpha_2 = 6$, and $|\chi_d| = 10^{-5}$. Panels (a) and (b) focus on the $0 \leq x \leq L/100$ region.

a few penetration depths, resembling the pre-solitonic excitations identified in the SG scenario, θ'_1 develops a tail reaching further into the segment bulk. In Fig. A.3(c), we can appreciate how the magnetic field, which originates from the edge-instability, is established at the speed of light within the segment's interior. Our simulation also keeps track of the field emitted by the multi-bilayer system, as it is obtained through the radiative boundary conditions in Eqs. (A.67) and (A.68), see the oscillations occurring at the two boundaries. Furthermore, we observe that, as a result of the field propagating symmetrically from both ends to the interior, a collision-like event unfolds around the center of the segment, leading to a standing-wave-type pattern. The magnitude of the latter profile is reasonably tied to the perfect geometry considered here, therefore we work with a phenomenological inter-bilayer damping coefficient α_2 to account for leaks in the cavity to the radiation field formed by the region between bilayers. We consider a rather substantial value of $\alpha_2 = 6$ to suppress these oscillatory transients, with negligible influence on our peak magnetic response, see below.

Effects of segment size, dielectric environment, and inter-bilayer damping. Figure A.3(c) highlights the traveling-wave nature of the total magnetic field in the multi-bilayer strip. In Figure A.4(a) we plot the length dependence of the ratio $\langle B_{\text{ind}}^{\text{max}} \rangle / |B_{\text{ext}}\chi_d|$. Even though the effect is triggered at the edges of the sample, it is relatively system size independent due to the fact that the magnetic field enhancement travels to the bulk of the sample. Starting from a constant in small segments, the peak response increases with length. The propagation in the bulk is ultimately limited, either by the pump pulse duration or by dissipation of the photon modes. This gives a new characteristic length-scale localizing the propagating mode, $l_{\text{loc}} = c/t_{\text{loc}}$ where $t_{\text{loc}} \sim \min\{\Delta t_{\text{pulse}}, 1/\alpha_2\}$. Beyond this length-scale, the maximum induced flux saturates to constant value. As a result, the magnetic field averaged over the segment falls off as $1/L$, as confirmed by the green dashed line in our plot. Another important point highlighted by Fig. A.4(a) is the universality in $|\chi_d|$. The accordance between the displayed data sets implies that $\langle B_{\text{ind}}^{\text{max}} \rangle / B_{\text{ext}}$ is proportional to $|\chi_d|$, which is in turn proportional to the local superfluid density n_s . This is shown also Fig. 5(b) in the main text, and it reflects the fact that our dynamical response originates from the pump acting on the equilibrium diamagnetic screening properties, which are indeed encoded in the susceptibility $|\chi_d|$, see the Appendix 2.

We now turn to a description of Fig. A.4(b), where we report time traces of $\langle B_{\text{ind}} \rangle / |B_{\text{ext}}\chi_d|$ for different values of the refraction index n , mimicking an interface to distinct dielectric environments. We observe that the overall magnitude of the system's response monotonically increases as the n parameter goes down. Indeed, as compared to the result for our standard choice of $n = 1$ throughout this work (marked here in orange), the peak average magnetic field shows a factor of 2 enhancement in the Neumann ($n \rightarrow 0$) limit, see the blue curve. Finally, in Fig. A.4(c), we address the effect of dissipation between bilayers by displaying time traces of $\langle B_{\text{ind}} \rangle / |B_{\text{ext}}\chi_d|$ computed by varying the α_2 coefficient. The latter quantity has minimal impact on the magnetic response's build-up and peak value. However, it plays a significant role in reducing the bounce-back oscillations observed as the system relaxes back to equilibrium.

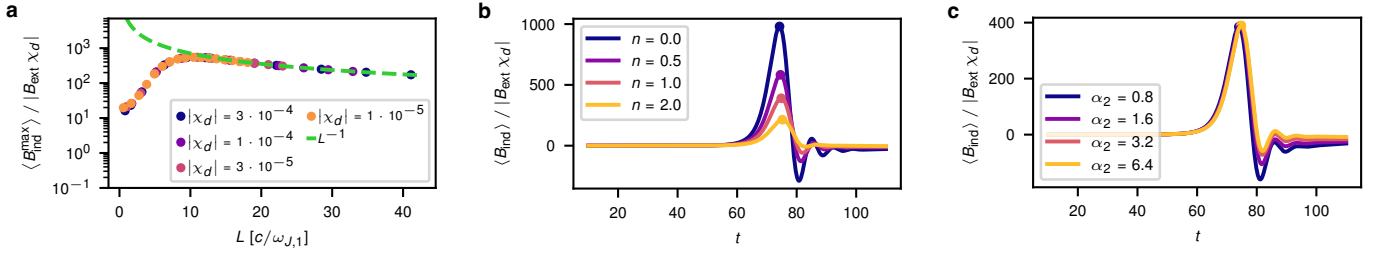


FIG. A.4. **Dependence on the L , n , and α_2 parameters.** **a** Dependence of the peak magnetic response ratio to the equilibrium diamagnetic field, $\langle B_{\text{ind}}^{\text{max}} \rangle / |B_{\text{ext}} \chi_d|$, where $\langle \dots \rangle$ stands for segment averaging, versus the segment size L . The traveling wave character illustrated in Fig. A.3(c) suggests that, although the instability stems from the edges, it is not strictly proportional to the number of edges, i.e., inversely proportional to L . It instead shows a peculiar length dependence due to the precise response of the excited bulk modes. For very large segment sizes, the magnetic field pulse cannot travel all the way inside the bulk, and the effect is localized to the boundary in space, over a length-scale determined by either the finite pump duration or the dissipation of the bulk modes. Beyond this point, the generated flux saturates, and the average magnetic field decays as $1/L$, see the green dashed line. The observed phenomenon is universal in $|\chi_d|$, as indicated by the accordance between the different sets of data points included the plot. Here the fixed parameters are: $V_0 = 3.5$, $\alpha_1 = 0.4$, and $\alpha_2 = 6$. **b** Time traces of the average induced magnetic field, normalized by the equilibrium diamagnetic field amplitude, for different values of the refraction index n of the dielectric environment, with fixed parameters $L = 3300\lambda$, $V_0 = 3.5$, $q = 2.3 \times 10^{-4}$, $\alpha_1 = 0.4$, $\alpha_2 = 6$, and $|\chi_d| = 10^{-5}$. The dielectric environment is seen to influence the peak response, with the largest value obtained in the Neumann limit of $n \rightarrow 0$. **c** Time-traces of the average induced magnetic field for different values of the inter-bilayer damping parameter α_2 , with fixed parameters $L = 3300\lambda$, $V_0 = 3.5$, $q = 2.3 \times 10^{-4}$, $\alpha_1 = 0.4$, $n = 1$, and $|\chi_d| = 10^{-5}$. The inter-bilayer dissipation strength has little effect on the reported magnetic field build-up and maximum, but it suppresses the bounce-back oscillations we observe in the time profiles due to Fabry-Pérot interferences.

APPENDIX 6: INDUCED MAGNETIC FIELD PROFILE BENEATH THE MASK

To estimate to what extent the magnetic field propagates from the pumped region to that beneath the mask, we make two main simplifying assumptions. First, the ensemble of illuminated edges is approximated as a 2D sheet of currents in the y - z plane, localized at defects along the x -direction and vanishing for $z > 0$, where the mask blocks the pumping field, see Fig. A.5(a). Second, the medium beyond the mask's edge is effectively described, at THz frequencies, via a dielectric constant consistent with the experiment³².

Here, we consider the geometry shown in Fig. A.5(a). The mask is placed at $z \geq 0$, whereas for $-z_{\text{spot}} < z < 0$ a single pumped edge at $x = 0$ is replaced by a sheet of dipole elements along the z -direction—extending over $-\infty < y < \infty$ by virtue of the above-assumed translational invariance across y —via a suitable averaging procedure over YBCO's unit cell. Our objective is to evaluate, at time t , the total magnetic field, along the y -direction, at an observation point $(x, y = 0, z > 0)$ representing the detector. The magnetic field contribution coming from a generic dipole in the sheet features both near-field and far-field components, decaying as $1/R$ and $1/R^2$, respectively, with R being the distance from the dipole⁸⁰. The far-field contribution is proportional to the time derivative of the electrical current j_z , whereas the near-field one is proportional to j_z itself⁸⁰. We note that, in our case, we expect a Gaussian-like behavior for the quantity j_z , implying the far-field contribution to be zero-averaging in time. We thus focus on the near-field result in the following. We mention, however, that similar formulas are readily derived for the far-field case as well. The y -component of the total magnetic field reads

$$B(x, y = 0, z > 0, t) = \frac{\mu_0 x}{2\pi} \int_{-\infty}^0 dy_d \int_{-z_{\text{spot}}}^0 dz_d \frac{j_z(t - R/c)}{R^3}, \quad (\text{A.69})$$

where c is the speed of light in the material, $R = \sqrt{x^2 + y_d^2 + (z - z_d)^2}$ the distance between the observation point and the generic dipole element at location $(x = 0, y = y_d, z = z_d)$, and $j_z(t - R/c)$ the electrical current associated to each dipole, evaluated at the retarded time $t - R/c$ to account for the delayed contributions coming from the different sources in our geometry. To proceed further, we need to prescribe a time-dependence for the j_z function. A first, interesting case we address is the impulsive limit: $c j_z(t - R/c) = j_0 \delta(t - R/c)$. Here, j_0 encodes the details of our YBCO averaging and is representative of the system's response in the pumped region, and δ stands for the Dirac

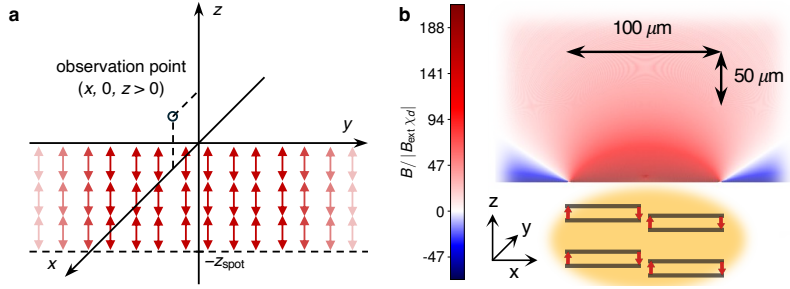


FIG. A.5. **Emitting edge currents and magnetostatic profile.** **a** Sketch of a current sheet, see the red arrows, extending over $-\infty < y < \infty$ and $-z_{\text{spot}} < z < 0$. The sheet is located at $x = 0$. We compute the total magnetic field at the point $(x, y = 0, z > 0)$. **b** Magnetostatic field distribution in the region beneath the mask, computed for a two-segment system, demonstrating how the edge currents lead to a paramagnetic profile that can penetrate deep into the mask.

delta function. By solving the double integral in Eq. (A.69), we get

$$B(x, 0, z > 0, t) = \begin{cases} 0, & \text{if } ct \leq \sqrt{x^2 + z^2}, \\ \frac{\mu_0 j_0}{2\pi} \frac{1}{c^2 t^2} \left[\arcsin\left(\frac{z+z_{\text{spot}}}{\sqrt{c^2 t^2 - x^2}}\right) - \arcsin\left(\frac{z}{\sqrt{c^2 t^2 - x^2}}\right) \right], & \text{if } ct > \sqrt{x^2 + z^2}. \end{cases} \quad (\text{A.70})$$

Rescaling the magnetic field by $\frac{\mu_0 j_0}{2\pi a} \equiv B_0$ (a quantity representative of the illuminated YBCO overall response), position by $a = ct_0 = 100 \mu\text{m}$, and time by $t_0 = 1 \text{ ps}$, we write

$$\frac{B(x, 0, z > 0, t)}{B_0} = \begin{cases} 0, & \text{if } t \leq \sqrt{x^2 + z^2}, \\ \frac{x}{t^2} \left[\arcsin\left(\frac{z+z_{\text{spot}}}{\sqrt{t^2 - x^2}}\right) - \arcsin\left(\frac{z}{\sqrt{t^2 - x^2}}\right) \right], & \text{if } t > \sqrt{x^2 + z^2}. \end{cases} \quad (\text{A.71})$$

The magnetic field profile for an arbitrary j_z function of time can be obtained by convolution with the impulsive response in Eq. (A.71). In the main text, we work with a multiple-sheet system, showing the results for a Gaussian-like profile centered around $t = 0$, with a standard deviation of 0.5, choosing $x = 0.4$, $z_{\text{spot}} = 1$, and various $z \sim 1$ values. More specifically, for the two-segment example we consider a profile of the form $j_z = \sum_{\lambda} j_0 \delta(x - x_{\lambda}) (-1)^{\lambda+1} \theta(-z) \theta(z + z_{\text{spot}}) \exp[-t^2/(2\sigma_t^2)]$, where even (odd) λ annotates right (left) edges, with $\sigma_t = 0.5$, $x_1 = 0$, $x_2 = L_{\text{seg}}$, $x_3 = L_{\text{seg}} + \delta x$, $x_4 = 2L_{\text{seg}} + \delta x$, $L_{\text{seg}} = 0.5$ (segments' length), and $\delta x = 0.01$ (separation between the two segments). The framework we employed compares reasonably well with the experimental counterpart³².

We conclude by addressing the result obtained upon convolving the impulsive response with a constant function—what we call the magnetostatic limit. In normalized units, we obtain the exact expression

$$\frac{B(x, 0, z > 0)}{B_0} = \arctan\left(\frac{z + z_{\text{spot}}}{x}\right) - \arctan\left(\frac{z}{x}\right). \quad (\text{A.72})$$

A similar formula is readily obtained for single and multiple YBCO segments (which involve a number of dipole sheets) by superimposing single-sheet magnetic field contributions. In Fig. A.5(b), we show the magnetostatic result for a two-segment system.

* marios.michael@mpsd.mpg.de

- [1] Basov, D. N., Averitt, R. D. & Hsieh, D. Towards properties on demand in quantum materials. *Nature Materials* **16**, 1077–1088 (2017). URL <https://www.nature.com/articles/nmat5017>.
- [2] de la Torre, A. *et al.* Colloquium: Nonthermal pathways to ultrafast control in quantum materials. *Reviews of Modern Physics* **93**, 041002 (2021). URL <https://link.aps.org/doi/10.1103/RevModPhys.93.041002>. Publisher: American Physical Society.
- [3] Bao, C., Tang, P., Sun, D. & Zhou, S. Light-induced emergent phenomena in 2d materials and topological materials. *Nature Reviews Physics* **4**, 33–48 (2022). URL <https://doi.org/10.1038/s42254-021-00388-1>.
- [4] Li, X. *et al.* Terahertz field-induced ferroelectricity in quantum paraelectric srtio3. *Science* **364**, 1079–1082 (2019). URL <https://doi.org/10.1126/science.aaw4913>.
- [5] Disa, A. S. *et al.* Photo-induced high-temperature ferromagnetism in ytio3. *Nature* **617**, 73–78 (2023). URL <https://doi.org/10.1038/s41586-023-05853-8>.

[6] Amano, T. *et al.* Light-induced magnetization driven by interorbital charge motion in the spin-orbit assisted mott insulator α -rucl₃. *Phys. Rev. Res.* **4**, L032032 (2022). URL <https://link.aps.org/doi/10.1103/PhysRevResearch.4.L032032>.

[7] Sriram, A. & Claassen, M. Light-induced control of magnetic phases in kitaev quantum magnets. *Phys. Rev. Res.* **4**, L032036 (2022). URL <https://link.aps.org/doi/10.1103/PhysRevResearch.4.L032036>.

[8] Siegrist, F. *et al.* Light-wave dynamic control of magnetism. *Nature* **571**, 240–244 (2019). URL <https://doi.org/10.1038/s41586-019-1333-x>.

[9] McIver, J. W. *et al.* Light-induced anomalous hall effect in graphene. *Nature Physics* **16**, 38–41 (2020). URL <https://doi.org/10.1038/s41567-019-0698-y>.

[10] Zong, A. *et al.* Ultrafast manipulation of mirror domain walls in a charge density wave. *Science Advances* **4**, eaau5501. URL <https://doi.org/10.1126/sciadv.aau5501>.

[11] Dolgirev, P. E., Michael, M. H., Zong, A., Gedik, N. & Demler, E. Self-similar dynamics of order parameter fluctuations in pump-probe experiments. *Phys. Rev. B* **101**, 174306 (2020). URL <https://link.aps.org/doi/10.1103/PhysRevB.101.174306>.

[12] Mitrano, M. *et al.* Possible light-induced superconductivity in k3c60 at high temperature. *Nature* **530**, 461–464 (2016). URL <https://doi.org/10.1038/nature16522>.

[13] Buzzi, M. *et al.* Phase diagram for light-induced superconductivity in κ -(ET)₂-X. *Phys. Rev. Lett.* **127**, 197002 (2021). URL <https://link.aps.org/doi/10.1103/PhysRevLett.127.197002>.

[14] Fausti, D. *et al.* Light-induced superconductivity in a stripe-ordered cuprate. *Science* **331**, 189–191 (2011). URL <https://doi.org/10.1126/science.1197294>.

[15] Chattopadhyay, S. *et al.* Mechanisms for long-lived, photo-induced superconductivity (2023). URL <https://arxiv.org/abs/2303.15355>.

[16] Eckhardt, C. J. *et al.* Theory of resonantly enhanced photo-induced superconductivity. *Nature Communications* **15**, 2300 (2024). URL <https://doi.org/10.1038/s41467-024-46632-x>.

[17] Kaiser, S. *et al.* Optically induced coherent transport far above T_c in underdoped yba₂cu₃o_{6+δ}. *Phys. Rev. B* **89**, 184516 (2014). URL <https://link.aps.org/doi/10.1103/PhysRevB.89.184516>.

[18] von Hoegen, A. *et al.* Amplification of superconducting fluctuations in driven yba₂cu₃o_{6+x}. *Phys. Rev. X* **12**, 031008 (2022). URL <https://link.aps.org/doi/10.1103/PhysRevX.12.031008>.

[19] Taherian, N. *et al.* Squeezed josephson plasmons in driven yba₂cu₃o_{6+x} (2024). URL <https://arxiv.org/abs/2401.01115>.

[20] Michael, M. H. *et al.* Parametric resonance of josephson plasma waves: A theory for optically amplified interlayer superconductivity in yba₂cu₃o_{6+x}. *Phys. Rev. B* **102**, 174505 (2020). URL <https://link.aps.org/doi/10.1103/PhysRevB.102.174505>.

[21] Michael, M. H. *et al.* Generalized fresnel-floquet equations for driven quantum materials. *Phys. Rev. B* **105**, 174301 (2022). URL <https://link.aps.org/doi/10.1103/PhysRevB.105.174301>.

[22] Ribak, A. *et al.* Two-fluid dynamics in driven yba₂cu₃o_{6.48}. *Phys. Rev. B* **107**, 104508 (2023). URL <https://link.aps.org/doi/10.1103/PhysRevB.107.104508>.

[23] Orenstein, J. & Dodge, J. S. Terahertz time-domain spectroscopy of transient metallic and superconducting states. *Phys. Rev. B* **92**, 134507 (2015). URL <https://link.aps.org/doi/10.1103/PhysRevB.92.134507>.

[24] Zhang, S. J. *et al.* Photoinduced nonequilibrium response in underdoped yba₂cu₃o_{6+x} probed by time-resolved terahertz spectroscopy. *Phys. Rev. X* **10**, 011056 (2020). URL <https://link.aps.org/doi/10.1103/PhysRevX.10.011056>.

[25] Babadi, M., Knap, M., Martin, I., Refael, G. & Demler, E. Theory of parametrically amplified electron-phonon superconductivity. *Phys. Rev. B* **96**, 014512 (2017). URL <https://link.aps.org/doi/10.1103/PhysRevB.96.014512>.

[26] Dai, Z. & Lee, P. A. Superconducting-like response in driven systems near the mott transition. *Phys. Rev. B* **104**, L241112 (2021). URL <https://link.aps.org/doi/10.1103/PhysRevB.104.L241112>.

[27] Dasari, N. & Eckstein, M. Transient floquet engineering of superconductivity. *Phys. Rev. B* **98**, 235149 (2018). URL <https://link.aps.org/doi/10.1103/PhysRevB.98.235149>.

[28] Sun, Z. & Millis, A. J. Transient trapping into metastable states in systems with competing orders. *Phys. Rev. X* **10**, 021028 (2020). URL <https://link.aps.org/doi/10.1103/PhysRevX.10.021028>.

[29] Dolgirev, P. E. *et al.* Periodic dynamics in superconductors induced by an impulsive optical quench. *Communications Physics* **5**, 234 (2022). URL <https://doi.org/10.1038/s42005-022-01007-w>.

[30] Okamoto, J.-i., Cavalleri, A. & Mathey, L. Theory of enhanced interlayer tunneling in optically driven high- T_c superconductors. *Phys. Rev. Lett.* **117**, 227001 (2016). URL <https://link.aps.org/doi/10.1103/PhysRevLett.117.227001>.

[31] Sentef, M. A., Kemper, A. F., Georges, A. & Kollath, C. Theory of light-enhanced phonon-mediated superconductivity. *Phys. Rev. B* **93**, 144506 (2016). URL <https://link.aps.org/doi/10.1103/PhysRevB.93.144506>.

[32] Fava, S. *et al.* Magnetic field expulsion in optically driven yba₂cu₃o_{6.48}. *Nature* **632**, 75–80 (2024). URL <https://doi.org/10.1038/s41586-024-07635-2>.

[33] Nicoletti, D. *et al.* Optically induced superconductivity in striped la_{2-x}ba_xcuo₄ by polarization-selective excitation in the near infrared. *Phys. Rev. B* **90**, 100503 (2014). URL <https://link.aps.org/doi/10.1103/PhysRevB.90.100503>.

[34] Likharev, K. K. *Dynamics of Josephson junctions and circuits* (Routledge, 1986).

[35] Ustinov, A. Solitons in josephson junctions. *Physica D: Nonlinear Phenomena* **123**, 315–329 (1998). URL <https://www.sciencedirect.com/science/article/pii/S0167278998001316>.

[36] Cuevas-Maraver, J., Kevrekidis, P. G. & Williams, F. *The sine-Gordon Model and its Applications* (Springer, 2014).

[37] Malomed, B. A. Soliton models: Traditional and novel, one- and multidimensional. *Low Temp. Phys.* **48**, 856–895 (2022).

[38] De Santis, D., Guarcello, C., Spagnolo, B., Carollo, A. & Valenti, D. Noise-induced, ac-stabilized sine-gordon breathers:

Emergence and statistics. *Commun. Nonlinear Sci. Numer. Simul.* **131**, 107796 (2024).

[39] De Santis, D., Spagnolo, B., Carollo, A., Valenti, D. & Guarcello, C. Heat-transfer fingerprint of josephson breathers. *Chaos, Solitons & Fractals* **185**, 115088 (2024). URL <https://www.sciencedirect.com/science/article/pii/S0960077924006404>.

[40] Neuenhahn, C., Polkovnikov, A. & Marquardt, F. Localized phase structures growing out of quantum fluctuations in a quench of tunnel-coupled atomic condensates. *Phys. Rev. Lett.* **109**, 085304 (2012).

[41] Lovas, I. *et al.* Many-body parametric resonances in the driven sine-gordon model. *Phys. Rev. B* **106**, 075426 (2022).

[42] Wybo, E., Bastianello, A., Aidelburger, M., Bloch, I. & Knap, M. Preparing and analyzing solitons in the sine-gordon model with quantum gas microscopes. *Phys. Rev. X Quantum* **4**, 030308 (2023).

[43] Kokanović, I., Cooper, J. R. & Iida, K. Changes in the in- and out-of-plane magnetic susceptibility of ybco crystals with temperature and hole content. *Europhysics Letters* **98**, 57011 (2012). URL <https://dx.doi.org/10.1209/0295-5075/98/57011>.

[44] Uemura, Y. J. *et al.* Universal correlations between T_c and $\frac{n_s}{m^*}$ (carrier density over effective mass) in high- T_c cuprate superconductors. *Phys. Rev. Lett.* **62**, 2317–2320 (1989). URL <https://link.aps.org/doi/10.1103/PhysRevLett.62.2317>.

[45] Emery, V. & Kivelson, S. Importance of phase fluctuations in superconductors with small superfluid density. *Nature* **374**, 434–437 (1995).

[46] Fertig, H. Deconfinement in the two-dimensional xy model. *Physical review letters* **89**, 035703 (2002).

[47] Babaev, E. Vortex matter, effective magnetic charges, and generalizations of the dipolar superfluidity concept in layered systems. *Phys. Rev. B* **77**, 054512 (2008). URL <https://link.aps.org/doi/10.1103/PhysRevB.77.054512>.

[48] Homann, G., Michael, M. H., Cosme, J. G. & Mathey, L. Dissipationless counterflow currents above T_c in bilayer superconductors. *Phys. Rev. Lett.* **132**, 096002 (2024). URL <https://link.aps.org/doi/10.1103/PhysRevLett.132.096002>.

[49] Kasper, V. *et al.* Simulating a quantum commensurate-incommensurate phase transition using two raman-coupled one-dimensional condensates. *Phys. Rev. B* **101**, 224102 (2020). URL <https://link.aps.org/doi/10.1103/PhysRevB.101.224102>.

[50] Lazarides, A., Tielemans, O. & Morais Smith, C. Pokrovsky-talapov model at finite temperature: A renormalization-group analysis. *Phys. Rev. B* **80**, 245418 (2009). URL <https://link.aps.org/doi/10.1103/PhysRevB.80.245418>.

[51] Majedi, A. H. Microwave-induced inverse faraday effect in superconductors. *Phys. Rev. Lett.* **127**, 087001 (2021). URL <https://link.aps.org/doi/10.1103/PhysRevLett.127.087001>.

[52] De Santis, D., Michael, M., Demler, E. & Lee, P. propagating-field-YBCO (2025). URL <https://doi.org/10.5281/zenodo.15011378>.

[53] Cavalleri, A. *et al.* Ongoing work (2024).

[54] McIver, J. W. *et al.* Light-induced anomalous Hall effect in graphene. *Nature Physics* **16**, 38–41 (2020). URL <http://dx.doi.org/10.1038/s41567-019-0698-y>. 1811.03522.

[55] Choi, D. *et al.* Direct observation of floquet-bloch states in monolayer graphene (2024). URL <https://arxiv.org/abs/2404.14392>. 2404.14392.

[56] Shimano, R. & Tsuji, N. Higgs mode in superconductors. *Annual Review of Condensed Matter Physics* **11**, 103–124 (2020). URL <https://www.annualreviews.org/content/journals/10.1146/annurev-conmatphys-031119-050813>.

[57] Haque, S. R. U. *et al.* Terahertz parametric amplification as a reporter of exciton condensate dynamics. *Nature Materials* **23**, 796–802 (2024). URL <http://dx.doi.org/10.1038/s41563-023-01755-2>. 2304.09249.

[58] Dai, Z. & Lee, P. A. Superconductinglike response in a driven gapped bosonic system. *Phys. Rev. B* **104**, 054512 (2021). URL <https://link.aps.org/doi/10.1103/PhysRevB.104.054512>.

[59] Lustig, E. *et al.* Photonic time-crystals - fundamental concepts. *Opt. Express* **31**, 9165–9170 (2023). URL <https://opg.optica.org/oe/abstract.cfm?URI=oe-31-6-9165>.

[60] Dubroka, A. *et al.* Evidence of a precursor superconducting phase at temperatures as high as 180 k in $rba_2cu_3o_{7-\delta}$ ($r = Y, Gd, Eu$) superconducting crystals from infrared spectroscopy. *Phys. Rev. Lett.* **106**, 047006 (2011). URL <https://link.aps.org/doi/10.1103/PhysRevLett.106.047006>.

[61] Uykur, E., Tanaka, K., Masui, T., Miyasaka, S. & Tajima, S. Persistence of the superconducting condensate far above the critical temperature of $yba_2(Cu, Zn)_3o_y$ revealed by c-axis optical conductivity measurements for several zn concentrations and carrier doping levels. *Phys. Rev. Lett.* **112**, 127003 (2014). URL <https://link.aps.org/doi/10.1103/PhysRevLett.112.127003>.

[62] Michael, M., Demler, E. & Lee, P. A. *to be published*.

[63] Lee, P. A., Nagaosa, N. & Wen, X.-G. Doping a mott insulator: Physics of high-temperature superconductivity. *Reviews of modern physics* **78**, 17–85 (2006).

[64] Wu, W. *et al.* Pseudogap and fermi-surface topology in the two-dimensional hubbard model. *Physical Review X* **8**, 021048 (2018).

[65] Lee, P. A. Amperean pairing and the pseudogap phase of cuprate superconductors. *Physical Review X* **4**, 031017 (2014).

[66] Agterberg, D. F. *et al.* The physics of pair-density waves: cuprate superconductors and beyond. *Annual Review of Condensed Matter Physics* **11**, 231–270 (2020).

[67] Niu, J. *et al.* Equivalence of pseudogap and pairing energy in a cuprate high-temperature superconductor. *arXiv preprint arXiv:2409.15928* (2024).

[68] De Santis, D. *et al.* Ongoing work (2024).

[69] Halperin, B. I. & Nelson, D. R. Resistive transition in superconducting films. *Journal of Low Temperature Physics* **36**, 599–616 (1979). URL <https://doi.org/10.1007/BF00116988>.

[70] Bulaevskii, L. N., Zamora, M., Baeriswyl, D., Beck, H. & Clem, J. R. Time-dependent equations for phase differences and a collective mode in josephson-coupled layered superconductors. *Phys. Rev. B* **50**, 12831–12834 (1994). URL <https://link.aps.org/doi/10.1103/PhysRevB.50.12831>.

[71] Kleiner, R., Müller, P., Kohlstedt, H., Pedersen, N. F. & Sakai, S. Dynamic behavior of josephson-coupled layered structures. *Phys. Rev. B* **50**, 3942–3952 (1994). URL <https://link.aps.org/doi/10.1103/PhysRevB.50.3942>.

[72] van der Marel, D. & Tsvetkov, A. A. Transverse-optical josephson plasmons: Equations of motion. *Phys. Rev. B* **64**, 024530 (2001). URL <https://link.aps.org/doi/10.1103/PhysRevB.64.024530>.

[73] Koyama, T. Quantum charge dynamics in an array of intrinsic josephson junctions. *Journal of the Physical Society of Japan* **70**, 2114–2123 (2001). URL <https://doi.org/10.1143/JPSJ.70.2114>. <https://doi.org/10.1143/JPSJ.70.2114>.

[74] Gabriele, F., Udina, M. & Benfatto, L. Non-linear terahertz driving of plasma waves in layered cuprates. *Nature Communications* **12**, 752 (2021).

[75] Gabriele, F., Castellani, C. & Benfatto, L. Generalized plasma waves in layered superconductors: A unified approach. *Phys. Rev. Res.* **4**, 023112 (2022). URL <https://link.aps.org/doi/10.1103/PhysRevResearch.4.023112>.

[76] Sellati, N., Gabriele, F., Castellani, C. & Benfatto, L. Generalized josephson plasmons in bilayer superconductors. *Phys. Rev. B* **108**, 014503 (2023). URL <https://link.aps.org/doi/10.1103/PhysRevB.108.014503>.

[77] Koshelev, A. Plasma resonance and remaining josephson coupling in the “decoupled vortex liquid phase” in layered superconductors. *Physical Review Letters* **77**, 3901 (1996).

[78] De Santis, D., Michael, M., Demler, E. & Lee, P. driven-YBCO (2024). URL <https://doi.org/10.5281/zenodo.13957684>.

[79] Eckardt, A. & Anisimovas, E. High-frequency approximation for periodically driven quantum systems from a floquet-space perspective. *New Journal of Physics* **17**, 093039 (2015). URL <https://dx.doi.org/10.1088/1367-2630/17/9/093039>.

[80] Feynman, R. P., Leighton, R. B. & Sands, M. *The Feynman Lectures on Physics*, vol. 1-3 (Addison-Wesley, Reading, Massachusetts, 1964). Available online: <https://www.feynmanlectures.caltech.edu/>.